

Net primary production in the Labrador Sea between 2014 and 2022 derived from ocean colour remote sensing based on ecological regimes

E. Devred^{a,*}, S. Clay^a, M. Ringuette^a, T. Perry^a, M. Amirian^{b,c}, A. Irwin^b, Z. Finkel^c

^a Fisheries and Oceans Canada, Bedford Institute of Oceanography, Dartmouth, NS, Canada

^b Department of Oceanography, Dalhousie University, Halifax, NS, Canada

^c Department of Mathematics and Statistics, Dalhousie University, Halifax, NS, Canada

ARTICLE INFO

Edited by Menghua Wang

Keywords:

Primary production
Labrador Sea
Phytoplankton assemblage
Oceanographic regimes
Phaeocystis spp.

ABSTRACT

Phytoplankton play a major role in carbon export and storage in the ocean interior through remineralization of particulate carbon into dissolved inorganic carbon (DIC), and represent the “gain” side of the biological carbon pump. Shifts in phytoplankton community structure and species succession impact primary production, quality of food for zooplankton consumers and the fate of organic matter in marine ecosystems.

In the Labrador Sea (LS), a sub-arctic environment, the emergence of large blooms of *Phaeocystis* spp. in spring at the expenses of diatoms may disrupt phytoplankton species succession with drastic consequences on the carbon cycle and the functioning of the marine ecosystem as these small flagellates aggregate in colonies of up to several millimeters, embedded in gelatinous matrices, that modify elemental stoichiometry, sinking rates and transfer of energy to higher trophic levels. In this study, we develop an ecological approach to estimate primary production due to *Phaeocystis* sp. in the LS from satellite remote sensing data. We used a regionally-tuned primary production model to assign phytoplankton photosynthesis efficiency as a function of oceanographic regimes defined by phytoplankton community structure and biomass, and sea-surface temperature. We found that four oceanographic regimes corresponded to broad phytoplankton taxonomic assemblages and environmental factors in the LS: the diatom-dominated Shelf, the low chlorophyll-a Basin, the mesotrophic Basin regimes and a last oceanographic regime within the Basin, where the flagellated prymnesiophyte *Phaeocystis* spp. likely dominated the assemblage. Annual primary production in the Labrador Sea varied between 200 and 300 Tg of carbon between 2014 and 2022 in agreement with previous studies. While *Phaeocystis* spp. contributed about 10 % of the annual production, two unusual blooms that occurred in 2015 and 2022 contributed about 14 and 20 % of total production, respectively. During these two events *Phaeocystis* sp. contributed 40 % and 60 % to the May production and extended over more than half the Labrador Sea. Spring blooms dominated by *Phaeocystis* may occur more frequently due to climate change and have the potential to impact the fate of carbon and alter the functioning of the LS ecosystem.

1. Introduction

The Labrador Sea (LS) plays a major role in the ventilation of the global ocean through winter deep convection that transports oxygen and carbon dioxide (CO_2) absorbed from the atmosphere into the surface to the deep ocean. Another pathway that removes absorbed CO_2 from the upper ocean is the biologically-driven removal of photosynthetically-fixed dissolved inorganic carbon from the upper ocean layers (Volk and Hoffert, 1985). However, the LS is undergoing significant changes as a result of global warming, including freshening that is likely to have consequences for deep water formation (Yashayaev and Loder, 2016;

Rühs et al., 2021; Clément et al., 2023), nutrients budget and primary production (Tesdal et al., 2022). Phytoplankton assemblage composition influences primary productivity and carbon export, with the accepted view that blooms of large phytoplankton, such as diatoms, are major contributors to carbon export while small phytoplankton, such as small flagellates, contribute to the microbial loop and the re-cycling of carbon in the near surface layers (Legendre and Le Fèvre, 1995). In fact, to be relevant to climatic scales (i.e., 100 years time), particulate carbon needs to be exported below the 1000-m isobath (Baker et al., 2022), which depends on the composition of the phytoplankton assemblage and the fate of organic matter produced in the euphotic zone (Balaguru et al.,

* Corresponding author.

E-mail address: emmanuel.devred@dfo-mpo.gc.ca (E. Devred).

2018). Phytoplankton spring blooms in the Northwest Atlantic are usually dominated by diatoms (Assmy and Smetacek, 2009), as has been observed in the LS (Fragoso et al., 2017, 2018). Warming of the North Atlantic may perturb diatom niches and species succession (Barton et al., 2016; Mutshinda et al., 2024), and favor small phytoplankton given their ability to harvest nutrients at low concentrations resulting from increased stratification, which hampers nutrient replenishment of the surface layer (Peter and Sommer, 2013). Increases in blooms of small phytoplankton such as the calcifying coccolithophores (e.g. *Emiliania huxleyi*) and dimethyl-sulfide producers (e.g. *Phaeocystis* spp.) have been documented in polar and subpolar environments (Oziel et al., 2020; Orkney et al., 2020) in response to climate change. To date, *Phaeocystis* spp. blooms in the LS have been recorded consistently on its eastern slope and shelf (Gieskes et al., 2007; Fragoso et al., 2017) as well as in several fjords of the Labrador coast (Simo-Matchim et al., 2017). However, the Atlantic Zone offshelf Monitoring Program, led by Fisheries and Oceans Canada, found high levels of *Phaeocystis* spp. aggregated in large colonies in the central and western Labrador Sea along the Atlantic Repeat Hydrography Line (AR7W) in 2015 and 2022 (Devred et al., 2024). Large bloom of *Phaeocystis* spp., especially when embedded in a gelatinous matrix, have implications for primary production and carbon export, since *Phaeocystis* spp. have high photosynthetic efficiencies (Lancelot and Mathot, 1987; Cota Glenn et al., 1994), show high carbon to chlorophyll-a ratios when in colonies (Smith et al., 2021; Smith and Trimborn, 2024) and may favor carbon export within the upper mesopelagic zone (~100 to 150 m) (Wang and Moore, 2011; Nissen and Vogt, 2021), although perhaps with limited export to the deep ocean due to microbial degradation (Reigstad and Wassmann, 2007; Smith and Trimborn, 2024).

Ocean colour satellites have been used to infer primary production at regional and global scales since their inception due to their high spatio-temporal sampling of the surface ocean (see for instance, Campbell and O'Reilly, 1988; Platt, 1986; Platt and Sathyendranath, 1988; Longhurst et al., 1995; Antoine et al., 1996; Lee et al., 1996; Behrenfeld and Falkowski, 1997). In particular, Sathyendranath et al., 1995, Longhurst (2007) and Harrison and Li (2015) assessed satellite-derived primary productivity in the LS using the Coastal Zone Colour Scanner (CZCS) and the Sea-viewing Wide Field-of-view Sensor (SeaWiFS). We note that computations by Sathyendranath et al. (1995) and Longhurst (2007) were carried out for a larger area than the LS, that was defined as the Polar Boreal biogeochemical province. The primary production models used in these studies were parameterised using photosynthetic parameters measured in the LS, making them fit for purpose at a coarse level. However, these studies applied a broad spatial (shelf vs. basin) and temporal (seasonal variation) statistical treatment of these photosynthetic parameters that may decrease the accuracy of PP estimates. In a warming climate that impacts phytoplankton phenology and community structure, which might in turn modify the photosynthetic efficiency of the phytoplankton assemblage (Fragoso et al., 2017; Fox et al., 2020), these approaches may be outdated. In the current study, we used information on the composition of phytoplankton assemblages, as revealed by pigment signatures, associated photosynthetic parameters, as derived from ^{14}C incubation experiments, and environmental factors collected in the LS between 2014 and 2022 to develop a satellite-based approach to infer photosynthetic parameters using ecological considerations. In particular, satellite-derived sea-surface temperature (SST) and chlorophyll-a concentration (Chl-a) were used to delineate the broad phytoplankton assemblages (e.g., diatom-dominated, *Phaeocystis*-dominated or mixed population) as revealed by pigment analysis, which in turn were used to derive community-specific photosynthetic parameters for our satellite-based primary production model. In this manuscript, we describe and assess the performance of the primary production model and report on primary production for two large blooms of *Phaeocystis* spp. that occurred in 2015 and 2022.

2. Data and method

2.1. Data and region of interest

2.1.1. Labrador Sea and AR7W

The region of study extends from 43 to 67 °W and from 51 to 67 °N for a total surface area of $1.6 \times 10^6 \text{ km}^2$. The data used in this study were collected along the AR7W transect, which was visited annually as part of the Atlantic Zone Off-shelf Monitoring program (AZOMP) between 2014 and 2022 (Table 1 and Fig. 1). Most of the missions occurred in May at the end of winter convection and before summer stratification, although due to logistic constraints, one mission occurred in June (2019) and one in July/August (2020), providing information on phytoplankton assemblages and production during summer. The AR7W routinely includes 28 stations where water samples are collected from surface to bottom using Niskin bottles attached to a rosette. Two types of stations were sampled during our study: HPLC stations (Fig. 1, black solid circle), where seawater was collected at four depths (1, 10, 25 and 100 m), and HPLC+PI stations (Fig. 1, open red circle), where seawater was collected at nine depths from surface to 100 m (2, 10, 20, 30, 40, 50, 60, 80, 100 m). In addition to the increased vertical resolution of sampling at the HPLC+PI stations, ^{14}C phytoplankton incubation measurements were carried out with water samples collected at two depths, the surface (i.e., 2 m) and the Chl-a maximum depth (as determined by the Fluorometer sensor mounted on the conductivity-temperature-density (CTD) system), which was generally located between 20 and 40 m. The CTD was deployed to the sea floor at each station. The number of biological stations per cruise varied between 5 and 7, and their locations were dictated by the timing of sampling to ensure that the water was collected early in the morning (ideally before 10 AM). The rosette was equipped with sensors that provided vertical profiles of temperature, salinity and fluorescence, among other properties, providing additional information to the Niskin bottle water samples. The CTD fluorescence was calibrated using Chl-a measured by fluorometry (Turner Design fluorometer) collected from the Niskin bottles at each station.

Phytoplankton pigment composition was determined for samples from the surface for the HPLC stations, and phytoplankton pigment composition and photosynthetic parameters (i.e., the production rate normalised to Chl-a, α^B ($\text{mg C} [\text{mg Chl-a}]^{-1} \text{ h}^{-1} [\text{W m}^{-2}]^{-1}$) and the maximum photosynthetic rate P_{max}^B ($\text{mg C} [\text{mg Chl-a}]^{-1} \text{ h}^{-1}$), see Section 2.2.2) were determined for samples collected at the surface and around 30-m depth for the HPLC+PI stations. For pigment composition measurements, immediately after collection, between 100 mL and 1000 mL of water was filtered on a GF/F 25 mm filter using a vacuum pump with a pressure lower than 10 PSI. The final volume was chosen after visually ensuring that enough material was collected on the filter. Filters were then flash frozen in liquid nitrogen and placed in a -80 °C freezer upon return to the Institute until laboratory analysis. Pigment concentrations were measured on an Agilent 1200 High Performance Liquid Chromatography (HPLC) system following the protocols of Head and Horne (1993) and Stuart and Head (2005). For taxonomic group identification, we used the following pigments in addition to Chl-a: chlorophyll-b (Chl-b), chlorophyll-c₃ (Chl-c₃), Fucoxanthin (Fuco),

Table 1

Date of AZOMP missions, N-HPLC corresponds to the number of stations where samples for HPLC analysis were collected and N_PI corresponds to the number of stations where ^{14}C incubation were conducted.

Year	Month	Start date	End Date	N_HPLC	N_PI
2014	May	May 7th	May 15th	35	7
2015	May	May 9th	May 16th	28	7
2016	May	May 7th	May 15th	30	7
2018	May	May 3rd	May 9th	25	6
2019	June	June 9th	June 21st	35	7
2020	July/August	July 29th	August 6th	29	0
2022	May	May 10th	May 20th	29	5

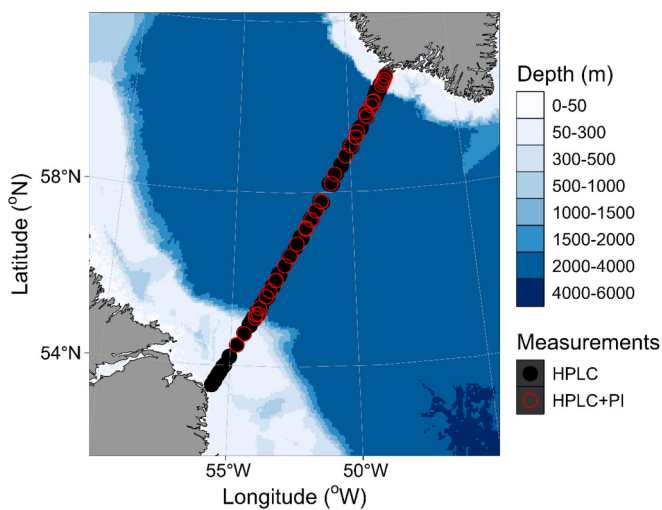


Fig. 1. Location of stations along the AR7W line categorized as follows: stations labeled HPLC indicate where phytoplankton pigments were measured, while stations labeled HPLC + PI indicate where both pigment measurements and incubation experiments were conducted.

19'-Butanoyloxyfucoxanthin (19-But), 19'-Hexanoyloxyfucoxanthin (19-Hex), peridinin (peri), Zeaxanthin (Zea), alloxanthin (allox). The biomass of eight taxonomic groups, namely, prasinophytes, dinoflagellates, cryptophytes, *Phaeocystis* spp., haptophytes (non-*Phaeocystis*), diatoms, dictyophytes and chlorophytes was calculated in each sample based on their pigment signature using the chemotaxonomic statistical analysis R package (Phytoclass) developed by Hayward et al., 2023. The results of the pigment analysis were validated using other method of phytoplankton identification including light microscopy, flow cytometry and image-based classification.(see Devred et al., 2024 for details). In addition, genomic analysis carried out on samples collected during an oceanographic mission occurring a week later in the vicinity of the AZOMP mission in 2022 indicated that the *Phaeocystis* spp. was the *P. pouchetii* species (R. Stevens-Green pers. comm.).

Photosynthetic parameters were derived from ^{14}C incubation experiments following the International Ocean Colour Coordinating Group protocol (IOCCG, 2022). Water from the surface and $\sim 30\text{-m}$ depth was collected in the morning. For each depth, a total of $30 \times 100\text{ mL}$ transparent glass bottles were filled with seawater, enriched with ^{14}C -bicarbonate and placed in a linear gradient white light incubator for 3 h with light ranging from 10 to $1255\text{ }\mu\text{mol photons m}^{-2}\text{ s}^{-1}$ for the surface samples and from 10 to $950\text{ }\mu\text{mol photons m}^{-2}\text{ s}^{-1}$ for samples collected at 30 m depth. Temperature in the incubator was kept at the appropriate in situ temperature, using a circulating refrigerated water bath. Following incubation, each bottle contents was filtered on to a GF/F 25 mm filter, which was immediately infused with pure HCl. The filters were placed in vials filled with scintillation fluid until analysis using a scintillation counter upon return to the Institute. Carbon uptake was plotted as a function of light intensity, to give a “photosynthesis-irradiance” (PI) curve, to derive photosynthetic parameters using an updated hyperbolic tangent formulation as described in Jassby and Platt (1976) (see Section 2.2.2).

The in situ dataset included a total of 283 HPLC samples (211 surface samples $<15\text{ m}$ and 72 collected between 15 and 40 m, referred to as “deep” samples), and 76 sets of photosynthetic parameters (39 surface values and 37 values collected between 20 and 40 m) derived from the ^{14}C experiments and referred to hereafter as PI parameters (see Section 2.2.2).

2.1.2. Satellite data

Daily 4-km resolution level-3 binned satellite products, namely remote sensing reflectance ($\text{Rrs}, \text{sr}^{-1}$), SST ($^{\circ}\text{C}$), and photosynthetically

active radiation (PAR, $\mu\text{mol photons m}^{-2}\text{ s}^{-1}$) from the MODIS-Aqua sensor were downloaded from the National Aeronautics and Space Administration (NASA) Ocean Biology Processing Group (OBPG, <https://oceancolor.gsfc.nasa.gov>) between 2014 and 2022, which corresponds to the period of in situ data collection. Chl-a (mg m^{-3}) was derived using a regionally-tuned version of the OC3M band-ratio algorithm (Clay et al., 2019). Gaps in Chl-a and SST were filled using the DINEOF method (Alvera-Azcarate et al., 2005, Sirjacobs et al., 2011; Hilborn and Costa, 2018, Liu and Wang, 2019) as provided on a github repository (<https://github.com/aida-alvera/DINEOF>, accessed on September 25th, 2024).

2.2. Methods

2.2.1. Pigment analysis and oceanographic regimes

Pigment compositions of surface samples ($N = 211$) were grouped using a cluster classification approach (*kmeans()* function in R, R Core Team, 2023). Pigments were normalised to Chl-a to avoid skewing the cluster analysis by trophic regime. The *NbClust()* function (R package mgcv, Charrad et al., 2014) was used to determine the optimum number of clusters. In brief, this function tests 30 different indices that indicate an optimum number of clusters and summarises the results according to the “majority rule”. In our case, six indices suggested two clusters, five indices suggested three clusters and three indices suggested seven clusters. We opted for seven clusters to ensure a wide representation of different taxonomic compositions as indicated by their pigment signature for different environments (Table 2). The same approach was used to group the “deep” samples (i.e., collected between 15 and 40 m, $N = 72$) according to their pigment signature normalised to Chl-a. The *Nbclust()* function returned an optimum number of 4 clusters for the deep samples (Table 3).

While this approach classified all pigment samples into seven broad taxonomic assemblage, it was not applicable to satellite observations, since ocean colour remote sensing cannot yet provide accurate measurements of individual phytoplankton pigments. Additional challenges include similarities (proximity in the dimensional space) of some cluster centers (Fig. S1, e.g., cluster # 2, 4, 7) and the spread of points within a cluster that may “overlap” with points from another cluster (Fig. S1). This is also noticeable when pigment samples were geolocated per cluster (Fig. S2.) showing that some clusters represented coastal waters (e.g., cluster #2) and others offshore waters (e.g., cluster #5 and #6) or a mixture of both (e.g., cluster #4). To circumvent these issues, a method was develop to infer taxonomic information from properties measured by ocean colour satellites (i.e., Chl-a and SST) by grouping clusters with similar environmental properties for the surface pigment samples using a decision tree (Fig. 2), assuming that each sample pigment grouping (i.e., cluster) would reflect a phytoplankton taxonomic assemblage with distinct mean temperature and Chl-a as discussed by Fragoso et al. (2016, 2017). In turn, retrieval of SST and Chl-a at a given satellite pixel would infer an oceanographic regime that predicts the broad taxonomic composition.

The analysis of the clusters, based on pigment signature, mean environmental properties, spatial extent, suggested four oceanographic regimes: 1) Low Chl-a Basin (LCB), 2) shelf regime dominated by diatoms (DDS), 3) a mixed population with a non-negligible presence of *Phaeocystis* spp. occurring in the Basin (MPB) and 4) a *Phaeocystis* spp. dominated regime also occurring in the Basin (HPB). Note that the HPB regime made of in situ samples with high biomass of *Phaeocystis* spp. was validated through comparison with phytoplankton abundance measured by light microscopy in 2014 and 2015, and notably, abundance of up to 10 millions of *Phaeocystis* spp. cells L^{-1} recorded in samples collected in 2015 (see Section 4.3 and Devred et al., 2024). The first step for the application of satellite imagery was to identify the DDS regime, which was achieved by selecting pixels in daily imagery with bathymetry $<2000\text{ m}$, with an additional temperature threshold to account for shifts in the Labrador and Greenland currents (e.g., Wang et al., 2016). Noting

Table 2

Cluster number, number of samples (number of estimates of PI parameters), mean and standard deviation of pigment ratios, Chl-a, sea-surface temperature, α^B and P_{max}^B for the 7 clusters resulting from the kmeans() analysis carried out on surface samples. Reported values are means \pm standard deviations.

Surface cluster	N (N_{PI})	Chl-b	Chl-c ₃	Fuco	Peri	Zea	Allo	19-But	19-Hex	Chl-a	Temp	$\alpha^B \times 10^{-2}$	P_{max}^B
1	26 (1)	0.125 \pm 0.115	0.007 \pm 0.017	0.035 \pm 0.048	0.000 \pm 0	0.006 \pm 0.017	0.019 \pm 0.031	0.002 \pm 0.010	0.059 \pm 0.062	0.30 \pm 0.19	3.90 \pm 3.61	7.9 \pm 0.0	3.33
2	37 (6)	0.027 \pm 0.048	0.027 \pm 0.040	0.351 \pm 0.058	0.002 \pm 0.010	0.001 \pm 0.004	0.005 \pm 0.012	0.003 \pm 0.011	0.016 \pm 0.031	3.29 \pm 2.79	1.95 \pm 1.85	9.9 \pm 8.2	5.94 \pm 5.27
3	15 (5)	0.516 \pm 0.121	0.028 \pm 0.064	0.178 \pm 0.043	0.005 \pm 0.019	0.002 \pm 0.007	0.009 \pm 0.025	0.032 \pm 0.051	0.137 \pm 0.067	0.54 \pm 0.45	2.13 \pm 2.15	6.4 \pm 1.8	2.50 \pm 0.41
4	48 (11)	0.016 \pm 0.032	0.044 \pm 0.049	0.225 \pm 0.033	0.004 \pm 0.024	0.000 \pm 0.000	0.002 \pm 0.009	0.002 \pm 0.013	0.049 \pm 0.065	1.70 \pm 1.32	2.42 \pm 2.09	9.5 \pm 5.7	5.75 \pm 3.32
5	25 (1)	0.040 \pm 0.052	0.054 \pm 0.055	0.131 \pm 0.083	0.006 \pm 0.016	0.000 \pm 0.000	0.004 \pm 0.010	0.001 \pm 0.007	0.273 \pm 0.066	0.65 \pm 0.51	7.78 \pm 2.95	7.9 \pm 0.0	3.83
6	27 (7)	0.250 \pm 0.067	0.140 \pm 0.083	0.231 \pm 0.061	0.000 \pm 0.000	0.004 \pm 0.010	0.001 \pm 0.003	0.057 \pm 0.036	0.174 \pm 0.074	1.19 \pm 0.61	2.75 \pm 1.58	9.2 \pm 11	5.16 \pm 4.51
7	33 (8)	0.003 \pm 0.016	0.260 \pm 0.079	0.259 \pm 0.045	0.000 \pm 0.0	0.000 \pm 0.000	0.000 \pm 0.000	0.003 \pm 0.016	0.036 \pm 0.053	3.27 \pm 2.12	2.52 \pm 1.14	6.2 \pm 2.0	4.52 \pm 1.51

Table 3

Cluster number, number of samples (number of estimates of PI parameters), mean and standard deviation of pigment ratio, Chl-a, temperature, α^B and P_{max}^B for the four clusters resulting from the kmeans() analysis carried out on deep samples. Reported values are means \pm standard deviations.

Deep cluster	N (N_{PI})	Chl-b	Chl-c ₃	Fuco	Peri	Zea	Allo	19-But	19-Hex	Chl-a	Temp	$\alpha^B \times 10^{-2}$	P_{max}^B
1	9 (6)	0.212 \pm 0.079	0.017 \pm 0.033	0.096 \pm 0.351	0.000 \pm 0.000	0.000 \pm 0.000	0.003 \pm 0.008	0.0210.026 0.045	0.045 \pm 0.043	0.47 \pm 0.11	1.20 \pm 2.38	5.0 \pm 1.5	2.73 \pm 0.43
2	26 (8)	0.025 \pm 0.054	0.075 \pm 0.105	0.760 \pm 0.977	0.000 \pm 0.000	0.004 \pm 0.016	0.001 \pm 0.007	0.000 \pm 0.000	0.014 \pm 0.047	2.35 \pm 2.88	1.62 \pm 2.59	17 \pm 13	8.23 \pm 5.36
3	27 (13)	0.100 \pm 0.092	0.099 \pm 0.082	0.248 \pm 0.183	0.023 \pm 0.45	0.001 \pm 0.007	0.011 \pm 0.017	0.014 \pm 0.033	0.179 \pm 0.135	1.05 \pm 0.56	4.32 \pm 1.29	5.0 \pm 1.3	3.67 \pm 0.95
4	10 (10)	0.000 \pm 0.000	0.912 \pm 0.789	0.789 \pm 0.714	0.000 \pm 0.000	0.000 \pm 0.000	0.000 \pm 0.000	0.007 \pm 0.022	0.067 \pm 0.105	2.88 \pm 2.37	2.82 \pm 1.08	7.0 \pm 2.2	4.99 \pm 1.06

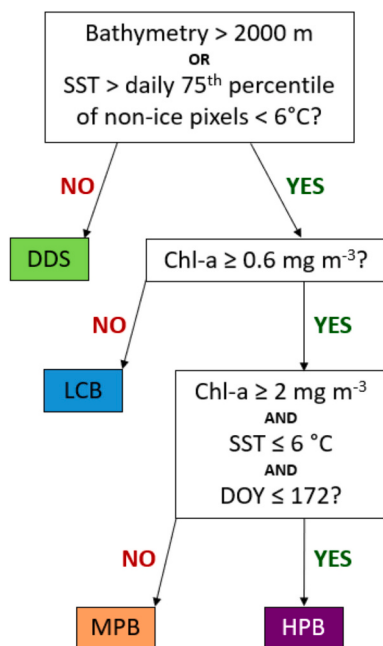


Fig. 2. Diagram of the pixel-based assignment of four oceanographic regimes using bathymetry, sea-surface temperature and sea-surface chlorophyll-a concentration for the Labrador Sea. DDS: Diatom-Dominated Shelf, LCB: Low Chl-a Basin, MPB: Mix-Phaeocystis Basin and HPB: High-Phaeocystis Basin.

that the shelf waters are colder than the Labrador Basin, a daily threshold derived from satellite-SST was used to reassign “warmer” pixels to the Central Labrador Sea (CLS). The DDS regime was delineated from other regimes using a combination of daily SST and bathymetry to allow for natural day-to-day variability in the boundary over the time series. First, ice-covered pixels were removed using the MASAM2 sea-ice concentration dataset (Fetterer et al., 2023), which was re-gridded onto the equidistant cylindrical grid used for the ocean colour data. Pixels exhibiting a sea-ice concentration greater than 70 % were removed from the analysis. Second, we computed the 75th percentile of SST for each day of the year for pixels where the bathymetry was shallower than 2000 m and SST was lower than 6 °C to generate a time series of daily shelf SST boundaries (Figure S1). This time series was smoothed using the *loess()* function in R with a span of 0.2 (a parameter that controls the degree of smoothing). Finally, pixels were assigned to the DDS regime regardless of their Chl-a if their SST values fell below this dynamic threshold and their bathymetry was shallower than 2000 m. This quality control prevented the occurrence of pixels identified as DDS from appearing in the CLS following eddy-induced upwellings.

The second step was to assign pixels located in the CLS to the three other regimes based on their Chl-a concentration: pixels with Chl-a $< 0.6 \text{ mg m}^{-3}$ were assigned to the LCB regime, pixels with Chl-a ranging from 0.6 to 2 mg m^{-3} were assigned to the MPB regime, and pixels with Chl-a $\geq 2 \text{ mg m}^{-3}$ were assigned to the HPB regime (Fig. 2). Finally, given that high *Phaeocystis* spp. biomass was not recorded in the in situ measurements after day of year 172 or when temperatures were higher than 6 °C (See Devred et al., 2024 for details relative to Figure S2), pixels classified as HPB in any image collected after day of year 172 or exhibiting a SST greater than 6 °C were reassigned to MPB.

Once all in situ samples were assigned to a regime, the mean properties of that regimes were computed (Table 4), with the mean PI

Table 4

Regime, number of samples (number of PI parameters), mean and standard deviation of pigment ratio, Chl-a, temperature, α^B and P_{max}^B for the four oceanographic regimes. Reported values are means \pm standard deviations.

Regime	N (N_{PI})	Chl-b	Chl-c3	Fuco	Peri	Zea	Allo	19But	19Hex	Chl-a	Temp	α^B $\times 10^{-22}$	P_{max}^B
DDS	56	0.081 \pm (10)	0.030 \pm 0.169	0.284 \pm 0.066	0.001 \pm 0.010	0.001 \pm 0.005	0.003 \pm 0.012	0.001 \pm 0.006	0.016 \pm 0.041	2.76 \pm 2.56	0.72 \pm 1.76	10.2 \pm 7.8	6.10 \pm 5.05
	70	0.131 \pm (11)	0.030 \pm 0.180	0.110 \pm 0.051	0.002 \pm 0.087	0.002 \pm 0.010	0.011 \pm 0.024	0.009 \pm 0.029	0.154 \pm 0.114	0.45 \pm 0.37	5.16 \pm 3.46	7.5 \pm 1.49	3.72 \pm 1.13
MPB	41	0.150 \pm (8)	0.125 \pm 0.126	0.229 \pm 0.076	0.004 \pm 0.025	0.002 \pm 0.007	0.001 \pm 0.045	0.037 \pm 0.041	0.133 \pm 0.090	1.18 \pm 0.55	3.37 \pm 1.14	8.9 \pm 10.2	5.04 \pm 4.21
	44	0.016 \pm (10)	0.193 \pm 0.039	0.283 \pm 0.119	0.003 \pm 0.071	0.001 \pm 0.003	0.002 \pm 0.005	0.005 \pm 0.017	0.048 \pm 0.057	3.20 \pm 1.83	3.03 \pm 0.91	7.0 \pm 4.1	4.85 \pm 2.12

parameters being used as inputs for the satellite-based primary production model (Section 2.2.2). The overall objective of the method is the assignment of photosynthetic parameters on a per-pixel basis. The approach does not provide information on phytoplankton species succession and should not been used as such even if it provides the likelihood of encountering a dominant phytoplankton taxonomic group in a given regime.

2.2.2. Satellite-based primary production

Photosynthetic parameters were derived from fitting the PI-curves using a recently developed formulation (<https://arxiv.org/abs/2412.17923>):

$$P^B = P_{max}^B \tanh\left(\frac{\alpha^B I}{P_{max}^B}\right) \tanh\left[\left(\frac{P_{max}^B}{\beta^B I}\right)^{2.38}\right], \quad (1)$$

Where I corresponds to the irradiance (W m^{-2}), P^B ($\text{mgC [mg Chl-a]}^{-1} \text{h}^{-1}$) is the production rate normalised to Chl-a, α^B ($\text{mgC [mg Chl-a]}^{-1} \text{h}^{-1} [\text{W m}^{-2}]^{-1}$) corresponds to the linear increase of carbon productivity at low light, P_{max}^B ($\text{mgC [mg Chl-a]}^{-1} \text{h}^{-1}$) corresponds the maximum specific photosynthetic rate, and β^B ($\text{mgC [mg Chl-a]}^{-1} \text{h}^{-1} [\text{W m}^{-2}]^{-1}$) corresponds to the photoinhibition rate. Note that the “B” superscript indicates normalisation to Chl-a. In absence of photo-inhibition ($\beta^B = 0$), Eq. (1) simplifies to the formulation of Jassby and Platt (1976). PI parameters from surface samples were then averaged for each oceanographic regime to generate regime-specific parameters that could be assigned to satellite pixels. The term accounting for possible photoinhibition was omitted in each regime as our analysis showed that only eight out of 39 (i.e., $\sim 20\%$) PI curves exhibited minor photo-inhibition and no satellite-derived approach accurately infers this term (<https://arxiv.org/abs/2412.17923>). The PI parameters for each regime were computed as the mean α^B and P_{max}^B for all in situ samples assigned to that regime (Table 4).

Satellite primary production PP ($\text{mg Carbon m}^{-2} \text{d}^{-1}$) was modelled as a function of the PI parameters α^B and P_{max}^B , spectrally-resolved irradiance between 400 and 700 nm (corresponding to PAR when integrated over the spectral range), and Chl-a. Depth-resolved PP was calculated at 0.5-m resolution down to the euphotic depth Z_{eu} (the depth at which PAR is 1 % surface PAR) with a one-hour time resolution over the photoperiod. The following paragraphs describe all the steps taken to compute daily PP in the model.

Hourly irradiance from 400 to 700 nm was computed at a 1-nm resolution was computed for the sea surface and just-below it using the Gregg & Carder model (Gregg and Carder, 1990) for a Maritime atmosphere. This simulated surface irradiance just above the sea surface was scaled such that its integration over a day and all wavelengths equals the daily PAR product obtained from the MODIS sensor. In the following paragraphs, the wavelength, λ (nm), was omitted for clarity.

Light attenuation for direct and diffuse components of surface irradiance, K_{dir} (Eq. 2) and K_{dif} (Eq. 3), was estimated at each depth as a function of the total absorption and backscattering in that layer:

$$K_{dir} = e^{-\Delta_z(a_t+b_{bt})/\cos(\theta_s)}, \quad (2)$$

$$K_{dif} = e^{-\Delta_z(a_t+b_{bt})/0.83}, \quad (3)$$

where Δ_z is the depth interval (0.5 m), θ_s is the solar zenith angle, and 0.83 is the average cosine of incoming diffuse irradiance (Sathyendranath and Platt, 1997). Total absorption (Eq. 4) and back-scattering (Eq. 5) coefficients were computed as the sum of individual optically-active components of the sea-water:

$$a_t = a_w + a_\phi + a_y, \quad (4)$$

$$b_{bt} = b_{bw} + b_{bp}, \quad (5)$$

where the absorption coefficient of pure sea water, a_w (m^{-1}), was given by Pope and Fry (1997) and the backscattering coefficient of pure sea water, b_{bw} (m^{-1}), was derived from Morel (1974). The phytoplankton absorption coefficient, a_ϕ (m^{-1}), was determined using the method from Devred et al. (2007) from an updated dataset with additional measurements collected by the Atlantic Zone and Atlantic Zone Off-Shelf Monitoring Programs. This dataset was used to calculate the photosynthetic action spectrum according to Kyewalyanga et al. (1997). The colored dissolved organic matter (CDOM) absorption coefficient, a_y (m^{-1}), was modelled as an exponentially decreasing function of wavelength (Bricaud et al., 1981) with a slope of 0.014. The particulate backscattering coefficient, b_{bp} was computed according to Hubert and Morel (1998) for particulate scattering, using the Ulloa et al. (1994) method to determine the ratio of backscattering to total scattering.

Irradiance (W m^{-2}) at depth z_n was then computed as the sum of the direct and diffuse components derived from the previous depth, z_{n-1} with $I_{dir}(0^-)$ and $I_{dif}(0^-)$ the values just below the surface computed from Gregg and Carder (1990):

$$I(z_n) = I_{dir}(z_{n-1})K_{dir} + I_{dif}(z_{n-1})K_{dif} \quad (6)$$

Primary production was modelled for all depths (i.e., surface to euphotic depth) and time of day (hour) using the formulation from Platt et al. (1991):

$$PP(z, t) = \frac{Ba^B I(z, t)}{\sqrt{1 + \left[\frac{a^B I(z, t)}{P_{max}^B}\right]^2}} \quad (7)$$

where B (mg m^{-3}) is the Chl-a concentration and $I(z, t)$ is the irradiance at time t (hr) and depth z (m) integrated over the visible spectrum. Total daily primary production was computed by integrating the hourly depth-resolved PP over the water column and then over the day ($\text{mg C}^{-2} \text{m}^{-2} \text{day}^{-1}$).

Both satellite and in situ primary production were computed using Eq. (6), but differ in their input. In situ PP was computed using the fluorescence profile recorded by the CTD system calibrated using Turner-derived Chl-a, while satellite-derived PP was computed assuming a uniform profile based on the median satellite-derived surface

Chl-a within 10 km of the sampling location. Satellite *PP* uses the mean surface average PI parameters computed for each oceanographic regime identified on a per-pixel basis from Chl-a and SST (Section 2.2.1 and Table 4) and assumes uniform Chl-a and PI parameters throughout the euphotic depth. In situ *PP* uses surface and deep PI parameters, where “surface” and “deep” water masses are separated by the mixed layer depth (computed as the depth where the density changes by 0.01 kg.m⁻³ as in Wijesekera and Gregg, 1996), and PI parameters are linearly interpolated from surface to the deep values and the deep value was taken to be constant below its depth.

3. Results

3.1. Taxonomic information, trophic regimes and photosynthetic parameters

3.1.1. Cluster analysis

The seven clusters derived from the pigment analysis of in situ samples were consistent with the known spatial distribution of phytoplankton assemblages in the Labrador Sea derived from both light-microscopy and chemotaxonomic identification (Fragoso et al., 2017). The pigment signatures of each cluster correspond to specific mean Chl-a, SST and photosynthetic parameters (Table 2). Clusters 2 and 7 present distinct pigment signatures with one or two pigment ratios that are markedly higher than the others. Cluster 2 exhibits the highest Fuco:Chl-a ratio (0.35) with relatively low values for the other pigment:Chl-a ratios, and the highest mean in situ surface Chl-a (3.29 mg m⁻³) and coldest mean temperature (1.95 °C). These characteristics of high biomass and low temperature correspond to environmental conditions that occur on the shelves (Labrador and Greenland; Harrison and Li, 2015) where the phytoplankton biomass is dominated by diatoms. Cluster 7 presents the highest Chl-c₃:Chl-a and Fuco:Chl-a ratios, both markers for *Phaeocystis* spp. (Jeffrey et al., 1997; Roy et al., 2011). This cluster exhibited some of the lowest pigment:Chl-a ratios for the other pigments among all clusters, suggesting that samples in this cluster were dominated by *Phaeocystis* spp.. This cluster also exhibited high mean in situ surface Chl-a (3.27 mg m⁻³). The samples in this cluster were mainly collected in 2015 across the CLS. The third distinct cluster is cluster 6, which exhibited the second highest Chl-c₃:Chl-a and Chl-b:Chl-a ratios. Chl-b is a marker for prasinophytes and chlorophytes, these two groups being differentiated by the presence of zeaxanthin in chlorophytes (Jeffrey et al., 1997; Roy et al., 2011). Given the high Chl-c₃:Chl-a ratio (0.231) and the presence of all other diagnostic pigments except peridinin, this cluster was identified as mixed-population with non-negligible abundance of *Phaeocystis* spp.. The remaining four clusters (1, 3, 4, and 5) showed the lowest mean Chl-a, except cluster 4 which had a mean in situ surface Chl-a of 1.70 mg m⁻³. These clusters show the pigment signature of “average” conditions of the LS, from low Chl-a waters (cluster 1) likely dominated by small flagellates (e.g. chlorophytes, cryptophytes) to mesotrophic environments when and where conditions are favorable for phytoplankton growth and diatoms represent a non-negligible part of the total biomass (e.g., cluster 4 with a Fuco:Chl-a ratio of 0.225). Note that cluster 4 exhibited the second lowest mean temperature (2.4 °C). Cluster 5 showed the highest mean temperature (7.78 °C), which is due to the late timing of sampling from mid-June to early August in 2019 and 2020 (Figure S5). The high ratio of 19-Hex:Chl-a suggests that haptophytes were the main taxonomic group in these samples. While *Phaeocystis* spp. also belong to the haptophyte taxonomic group, it is differentiated from other haptophytes by its Chl-c₃:Chl-a signature. The high 19-Hex concentration relative to Chl-a may also be explained by the ability of some haptophytes to produce 19-Hex, a photoprotective pigment, in high-light environment (E. Head, person. Comm.) as samples assigned to cluster 5 were collected in summer.

Clusters 2, 4, and 6 showed the highest values for the photosynthetic parameters, with mean α^B values of 0.099, 0.092 and 0.095, respectively

and mean P_{max}^B values of 5.94, 5.16 and 5.65, respectively (Table 2). The low Chl-a clusters (1 and 3) showed the lowest photosynthetic efficiency, while *Phaeocystis*-dominated samples (cluster 7) exhibited α^B and P_{max}^B values that lie between the previous clusters (0.062 and 4.52 respectively). The single sample in cluster 5 was collected in summer and had intermediate values for its photosynthetic parameters.

The deep samples were analysed independently of the surface ones to account for acclimation that may impact pigment ratios (and therefore chemotaxonomic classification) and photosynthetic efficiency. The 4 clusters for the deep samples showed pigment signatures and distributions similar to the 7 clusters found for the surface samples (Table 3). Cluster 2 for the deep samples showed a similar pattern to cluster 2 from the surface samples with a high Fuco:Chl-a ratio, high mean Chl-a, and low temperature. This cluster corresponds to the shelf environment dominated by diatoms. In a similar manner, Cluster 4 shows a pigment signature, Chl-a and temperature that were similar to those of cluster 7 for the surface samples, that were identified as having high *Phaeocystis* spp. levels. Finally, clusters 1 and 3 had the characteristics of low Chl-a and mixed-population regimes respectively. In fact, for a given station, in 88 % of the cases, the regime at depth matched the regime found at the surface after refining the classification based on temperature and geographic location.

3.1.2. From cluster classification to oceanographic regimes

The surface clusters derived from the in situ samples were based on pigment signature, bathymetry, satellite-derived SST and Chl-a to define four oceanographic regimes, which in turn may be identifiable using satellite observations of Chl-a and SST (Fig. 2). A two-step approach was used 1) to group clusters with similar characteristics, and 2) to re-assign some in situ samples to a given oceanographic regime based on their temperature and the bathymetry at the sampling location (Fig. 2). In situ samples in clusters 1, 3, 4, and 5 which exhibited the warmest temperatures, the lowest Chl-a and were mainly located in the Labrador Basin (Figure S3), were grouped into a single regime, namely the *LCB* regime. Pigment distribution in this regime exhibited the highest Chl-b:Chl-a and some of the lowest Chl-c₃:Chl-a ratios (Table 4) indicating a signature (pigment and oceanographic conditions) of the “normal” conditions in the Labrador Sea in 2014, 2016, 2018, 2019 and 2020 (Fragoso et al., 2017, cluster C3b in Fig. 4 of their manuscript). Cluster 2 samples were mainly located on the shelves (Figure S3) and showed the highest Fucoxanthin:chl-a ratios and constituted the diatom-dominated shelf (*DDS*) regime. Cluster 6 samples came from the Basin (Figure S3) and had relatively high Chl-c₃ and Fucoxanthin to Chl-a ratios representing a regime with non-negligible biomass of *Phaeocystis* spp. along with other phytoplankton groups that also contains Fucoxanthin such as diatoms. This cluster corresponds to the mixed-population regime and is referred to as *MPB*. Cluster 7, which exhibited high mean Chl-a, the highest Chl-c₃:Chl-a and Fuco:Chl-a ratios, and some of the lowest remaining pigment ratios, was labeled *HPB* to denote high concentrations of primarily *Phaeocystis* spp.. Samples in this cluster were mainly located in the Basin with a few samples on the Greenland Shelf. Application of the classification scheme (Fig. 2) to the cluster re-arrangement provided a robust delineation of the shelf and basin regimes (Figure S4).

The *DDS* regime showed a colder average temperature than the three other regimes (Fig. 3b) with a notable separation at around 2 °C in the in situ dataset. Both *MPB* and *HPB* regimes showed overlapping temperature distributions, while the *LCB* regime showed a bi-modal temperature distribution which is explained by the timing of sampling (from spring to summer). The temperature distribution supports the separation of the shelves and the basin based on sea-surface temperature, although, given the limited seasonal coverage of the in situ dataset, a constant threshold of 2 °C does not seem appropriate for the application of satellite methodology. Thus, we created a dynamic threshold from daily satellite SST to account for the seasonal cycle of sea-surface temperature in the LS. The first assumption was that the *DDS* regime was restricted within the

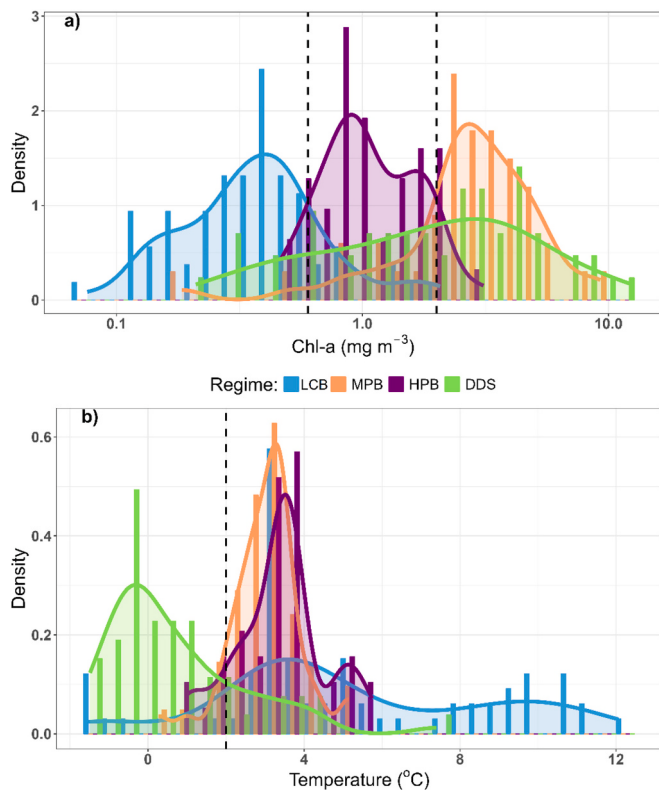


Fig. 3. Density function of a) Chl-a and b) surface temperature for the four oceanographic regimes derived from the in situ dataset. The two vertical dashed lines in panel a) correspond to the Chl-a boundaries used to delineate the three non-Shelf regimes (0.6 and 2 mg m^{-3}) and the vertical dashed line in panel b) corresponds to the SST boundary that separates the Shelf from other regimes ($2 \text{ }^{\circ}\text{C}$) in the in situ dataset, while a dynamic threshold was used for the satellite data (Section 2.2.1).

2000-m isobath. The second assumption was that the “coldest” water within the 2000-m isobath in any daily SST image represented the shelf regime, with “coldest” being defined as all pixels with an SST lower than the 75th percentile of all SST within the 2000-m isobath. This provided a SST threshold that varied between 0 (March–April) to $6 \text{ }^{\circ}\text{C}$ (August–September) depending on season and year. While the temperature appeared to be a good indicator of the DDS regime, Chl-a was used to separate the three regimes occurring within the Labrador Basin (Fig. 3a). A threshold of 0.6 mg m^{-3} was used to separate the LCB regime from the MPB regime, and a threshold of 2 mg m^{-3} was used to identify the HPB regime.

3.1.3. Photosynthetic parameters assignment for satellite applications

Each of the regimes described in the previous section showed a different mean photosynthetic efficiency with the DDS regime exhibiting the highest α^B and P_{\max}^B (0.10 and 6.10 respectively) (Table 4). The MPB regime, likely dominated by both diatoms and *Phaeocystis* spp. was the second most productive regime (per unit of time and surface area). Finally, both HPB and LCB regimes, likely dominated by small flagellates, had the lowest α^B values (0.07 for both regimes) and P_{\max}^B values (4.8 and 3.7 for HPB and LCB regimes respectively).

3.2. Satellite-derived primary production

3.2.1. Modelled vs. in situ daily primary production estimates

In situ PP computation exhibited a wide range of values, from about $500 \text{ mg C m}^{-2} \text{ d}^{-1}$ to about $12,000 \text{ mg C m}^{-2} \text{ d}^{-1}$ with the lowest production occurring in the LCB regime and the highest, in the DDS regime. The lowest production occurred at low Chl-a (following the

spring bloom) in the DDS regime and at low Chl-a in the LCB regime, both occurring in early to mid-May 2014, while the highest production occurred at high Chl-a (12.3 mg m^{-3}) in late May 2022 in the DDS regime. A comparison between in situ and satellite-derived daily PP showed good overall agreement (Fig. 4) with slightly underestimated satellite estimates. The linear regression of \log_{10} -transformed satellite-derived PP against \log_{10} -transformed in situ PP had intercept and slope values of 0.22 and 0.9 respectively ($R^2 = 0.68$ and RMSLE = 0.27). The number of data points for a given regime (8 to 9 points) was too small to compute regime-based robust statistics, however, and most points within a regime remained close to the one to one line, with each regime exhibiting a few outliers, notably for the LCB regime at low PP values and the DDS regime at high PP values. Daily PP values computed with DINEOF-derived Chl-a (small circles) showed good agreement with the in situ data, supporting the use of this approach to fill missing Chl-a.

3.2.2. Interannual variability of satellite-derived daily PP

The first-order variation in daily primary production strongly follows the solar cycle with very low production in winter and a peak in late spring or early summer (Fig. 5). The second-order variation is modulated by phytoplankton biomass with the highest values occurring in the HPB (around $4000 \text{ mg m}^{-2} \text{ d}^{-1}$ with a peak at $6500 \text{ mg m}^{-2} \text{ d}^{-1}$ in 2021) and DDS regimes (around $3000 \text{ mg m}^{-2} \text{ d}^{-1}$ with a peak at $\sim 5500 \text{ mg m}^{-2} \text{ d}^{-1}$ in 2014). These regimes exhibited the highest phytoplankton biomass in spring, with a peak occurring on an average of day 131 and 140 for the DDS and HPB regimes respectively (i.e., mid-April). The LCB and MPB regimes peak later in the year around day 165 and 176 respectively (i.e., mid-June). While the MPB regime exhibits relatively high daily PP in summer with values of around $2000 \text{ mg C m}^{-2} \text{ d}^{-1}$ and maximum above $3000 \text{ mg C m}^{-2} \text{ d}^{-1}$, the LCB regime showed the lowest daily primary production with values always below $800 \text{ mg C m}^{-2} \text{ d}^{-1}$. The LCB regime also appeared to be the regime with the most regular seasonal cycle.

3.2.3. Annual primary production budget in the LS between 2014 and 2022 as derived from satellite measurements

Total primary production exhibited large interannual variations in the LS with carbon production ranging from 204 Tg of carbon (2014) to 301 Tg of carbon (2016) (Table 5 and Fig. 6). Most of the production occurred in the Labrador Basin and was driven by the MPB regime which accounted for between 31.7 % (2015) to more than 60 % (2016) of total annual production, with an average percent contribution of 43.4 %. The maximum contribution of the MPB regime in 2016 corresponded to the second smallest contribution to total production by the HPB regime; as expected as the increase in surface area (and therefore PP) of one of these regime occurs at the expense of the other. In 2015, the HPB regime

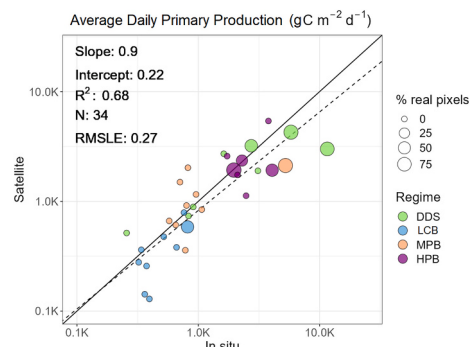


Fig. 4. Median daily satellite-derived PP within 10 km of the sampling location versus in situ PP for 34 measurements located within the Labrador Sea between 2014 and 2022. The solid line corresponds to the 1:1 line and the dashed line corresponds to the linear regression of satellite vs. in situ daily PP. The “% real pixels” term refers to the percentage of pixels within 10 km that had real satellite data, as opposed to DINEOF-filled values.

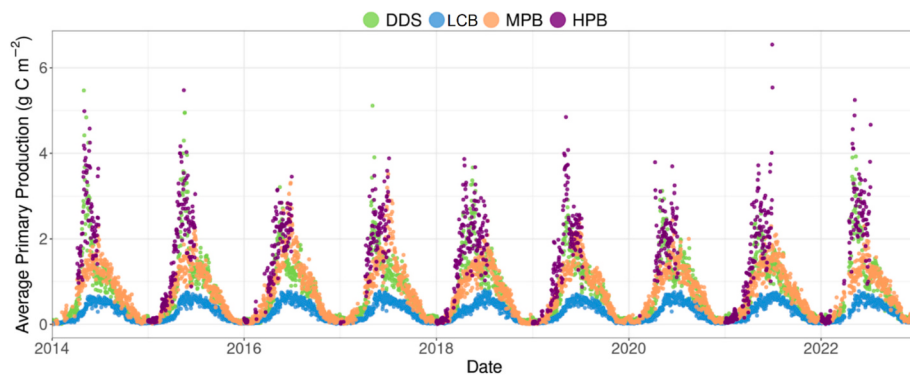


Fig. 5. Average daily primary production between 2014 and 2022 in the Labrador Sea for four oceanographic regimes derived from MODIS data.

Table 5

Annual primary production (Total Ann PP), Percentage contribution of a given regime to total annual primary production (% Ann. PP), Month at which a given regime reaches maximum production (Month Max PP), Month at which a given regime reaches its maximum production relative to other regimes (Month Max %), contribution of a given regime to monthly PP at its month of maximum relative contribution (% of PP at Monthly Maximum). For the HPB, the duration is the length of time in weeks that this regime covers more than 10 % of the LS surface area.

	Year	2014	2015	2016	2017	2018	2019	2020	2021	2022	Mean
	Total Ann. PP (Tg of C)	204	246	301	269	243	268	230	298	238	255
Regime											
DDS	% Ann. PP	22	24.4	20.5	21.7	26.3	25.3	28.7	26	25.6	24.5
	Month Max PP	May	May	Jun	Jul	July	Jun	May	May	May	–
	Month Max % Ann. PP	Dec	Sep	Dec	Dec	Oct	Dec	Nov	May	Nov	–
	% of PP at Monthly Maximum	44.5	33.1	44.0	55.1	39.7	46.6	47.2	35.6	35.3	–
LCB	% Ann. PP	31.5	23.8	12.4	17.7	22.5	20.1	26.6	16.3	24	21.7
	Month Max PP	Aug	Aug	Apr	Aug	Aug	Aug	Aug	Jun	Aug	–
	Month Max % Ann. PP	Mar	Mar	Feb	Feb	Feb	Feb	Feb	Mar	Mar	–
	% of PP at Monthly Maximum	90.5	88.5	89.3	83.5	86.3	78.1	77.6	67.1	89.4	–
MPB	% Ann. PP	33.2	31.7	60.3	52.3	39.5	47.9	37.4	51.8	36.5	43.4
	Month Max PP	Jun	Jun	Jul	Jul	Jul	Jun	Jul	Jun	–	–
	Month Max % Ann. PP	Jun	Jun	Jul	Jul	Jul	Jul	Jul	Jul	Oct	–
	% of PP at Monthly Maximum	55.1	47.2	77.9	75.3	64.9	70.1	53.4	71.9	54.4	–
HPB	% Ann. PP	13.4	20	6.78	8.28	11.7	6.57	7.2	5.89	13.9	10.4
	Month Max PP	May	May	May	May	Apr	May	Jun	May	May	–
	Month Max % PP	May	May	May	May	Apr	May	Jun	Apr	May	–
	% of PP at Monthly Maximum	47.3	60.3	27.3	30.7	45.2	30.2	18.2	21.4	46.8	–
Duration (weeks)											
5											

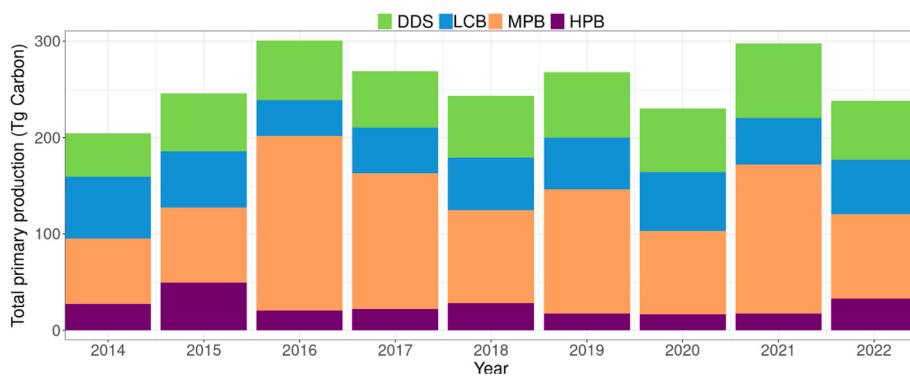


Fig. 6. Annual primary production budget (Tg Carbon) per regimes between 2014 and 2022.

contributed about 20 % of the total annual production, with a peak at 60 % of the LS monthly production in May in 2015 (Table 5 and Fig. 6). In general, the contribution by HPB regime remained at around 10 % or less of the total annual production and peaked in May, with the exception of 2018 and 2020 when it peaked in April and June respectively. The lowest contribution to total annual PP by the HPB regime occurred in 2021 with a value of 5.9 %. Primary production peaked in the LCB regime in August, except in 2016 and 2021 when it peaked in April and

June respectively, and its contribution to annual primary production ranged between 12.4 % (2016) and 26.6 % (2020) with an average percent contribution of 21.7 %. However, the highest contribution to monthly PP occurs in winter (February and March) and varies between 67 and 90 % of the monthly production. Finally, the DDS regime showed the least variation in the percent contribution to annual production and varying between 20.5 % (2016) and 28.7 % (2020) and peaking between May and July. Peak timing in both the MPB and HPB regimes

corresponded to their maximum contribution to annual PP, while the maximum contribution of the LCB regime occurred early in the year in February and March, and the maximum contribution of the DDS regime to annual primary production occurred in Fall (Table 5) and represent between 33 and 55 % of monthly PP.

Phaeocystis blooms have often been observed on the Greenland Shelf and Slope in the past (e.g. Stuart et al., 2000; Fragoso et al., 2016). In recent years, however, high biomass of *Phaeocystis* spp. has been recorded across the Labrador Basin. Under “normal” conditions (i.e., excluding 2014, 2015 and 2022), high *Phaeocystis* spp. biomass covers about $4.5 \times 10^6 \text{ km}^2$ at its peak, corresponding to about 14.1 % of the Labrador Sea surface area (Fig. 7). In 2014 and 2022, however, the *Phaeocystis* spp. bloom covered 6.4×10^6 and $7.9 \times 10^6 \text{ km}^2$ (22.8 and 26.8 % of the LS surface area) and a record surface area of $12.6 \times 10^6 \text{ km}^2$ was observed in 2015 (43.4 % of the LS), which is more than twice the average extent of high biomass *Phaeocystis* spp. during “normal” conditions. The duration of the HPB regime, defined as the number of weeks at which the percent cover of the HPB regime remains above 10 % of the total surface area of the LS, is comparable between years and the three widespread blooms of *Phaeocystis* spp. in 2014, 2015 and 2022 did not last longer than the “normal” *Phaeocystis* spp. blooms.

4. Discussion and conclusion

Here, we have adapted and validated a satellite-based primary production model (Platt and Sathyendranath, 1988; Platt et al., 2008) to provide annual estimates of primary production between 2014 and 2022. While previous satellite-based estimates of primary production in the LS have been published (Antoine et al., 1996; Behrenfeld and Falkowski, 1997; Platt et al., 2008; Ryan-Keogh et al., 2023), these were computed using globally-tuned models that underestimate bloom intensity in the LS (Clay et al., 2019). The present study uses Chl-a computed using regionally-tuned coefficients of a band-ratio algorithm (Clay et al., 2019) and constitutes a step forward in improving the accuracy of PP estimates in this important region, as well as documenting

the recent occurrences of large blooms of *Phaeocystis* spp. and their associated primary production.

4.1. Oceanographic regimes and photosynthetic parameters

The assignment of photosynthetic parameters from satellite remote-sensing is an arduous task, exacerbated in the Labrador Sea by the limited number of in situ measurements and the narrow temperature range, which prevents statistically-robust relationships between temperature and PI parameters (results not shown) such as those reported elsewhere (e.g., Eppley, 1972; Behrenfeld and Falkowski, 1997; Bouman et al., 2005; Robinson et al., 2018). Other approaches to derive primary production from satellite measurements rely on averaging all available PI parameters within a region of interest and applying this unique set of parameters to the PP model (e.g., Longhurst et al., 1995; Longhurst, 2007; Bélanger et al., 2013; van Oostende et al., 2023). Recently, Brewin et al. (2017) assigned photosynthetic parameters based on phytoplankton size distribution and computed satellite-derived PP along the Atlantic Meridional Transect, showing that picoplankton primary production was within the same order as that of large phytoplankton (i.e., nano- and micro-phytoplankton, $> 2 \mu\text{m}$). The method used in the current study is similar to that reported by Devred et al. (2007), which used satellite-based SST and Chl-a to delineate Longhurst (2007) biogeographical provinces in the Northwest Atlantic and assigned PI parameters by province. In that study, the Labrador Sea was divided in two biomes: the Labrador Basin and the shelves, a method that was also used by Harrison and Li (2015). Our approach, which was based on phytoplankton pigment signatures, total phytoplankton biomass, and SST, provides a more detailed partition of the Labrador Sea based on ecological considerations, in particular, the composition of the different phytoplankton assemblages.

Stuart et al. (2000), Sathyendranath et al. (2001) and Fragoso et al. (2017) used chlorophyll-c₃ as an indicator of the presence of the prymnesiophyte *Phaeocystis* spp. in the LS. The Chl-c₃:Chl-a and Fuco:Chl-a ratios found in the HPB regime (Table 4) were similar to the

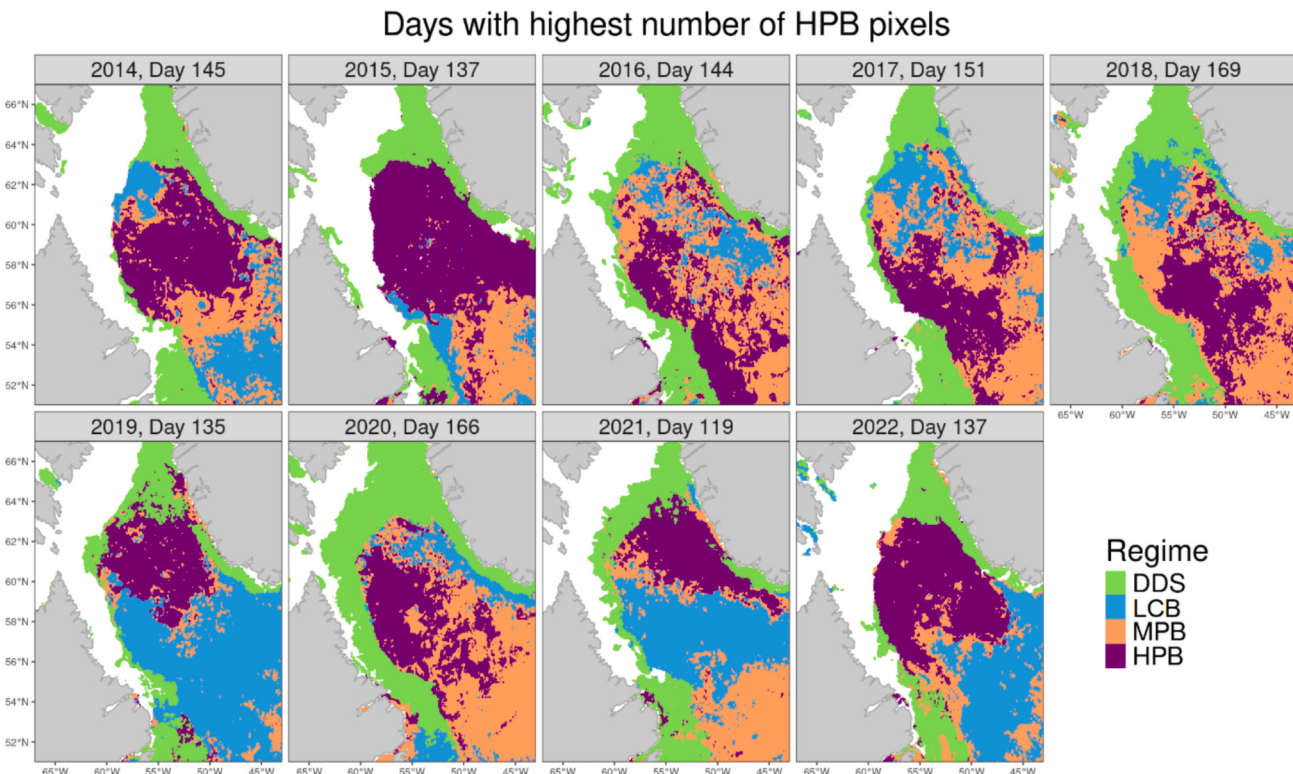


Fig. 7. Spatial distribution of oceanographic regimes at the peak extent of *Phaeocystis* spp. bloom (i.e., HPB regime) by year.

ratios found by Fragoso et al. (2017) who used the CHEMTAX approach for pigment-based taxonomic classification of water samples in the LS from 2005 to 2014, where the highest biomass contribution by *Phaeocystis* spp. was about 70 % (See Fragoso et al., 2017, Fig. 3d). A detailed chemotaxonomic analysis of the pigment signatures of water samples used in this study showed that the percentage of *Phaeocystis* spp. in the total biomass was as high as 90 % in 2015 and light-microscopy showed the abundance of *Phaeocystis* spp. was higher than 10 million cells per liter (Devred et al., 2024). The Chl-a threshold of 2 mg m^{-3} used to distinguish high *Phaeocystis* spp. biomass, and therefore the HPB regime, from a mixed-population of phytoplankton where both diatoms and *Phaeocystis* spp. may co-exist (MPB regime) is in agreement with the one found by Harrison and Li (2015) on the Greenland Shelf using satellite ocean colour data collected between 1991 and 2011 to identify blooming conditions on the Greenland Shelf with *P. pouchetii* identified as the dominant phytoplankton. The pigment signature of the MPB regime reveals the likely presence of both diatoms and *Phaeocystis* spp., along with other taxonomic groups as indicated by the relatively high ratios of Chl-b, 19'-Hex and 19'-But to Chl-a. These latter pigments are markers for prasinophytes, chlorophytes, haptophytes, and cryptophytes as highlighted in Fragoso et al. (2017). It is noteworthy, however, that while Fragoso et al. (2017) found that the occurrence of *Phaeocystis* spp. was limited to the Greenland Shelf and Slope, while our study shows that the genus has spread more recently to the center of the LS and even to its western part in 2015.

Ultimately, this approach did not aim at providing a detailed description of the phytoplankton community structure and species succession but rather provided a broad view of the trophic regimes that can be detected using satellite remote-sensing. In that respect, it is possible that in some years, diatoms may make a non-negligible contribution to total biomass in the HPB and MPB regimes and *Phaeocystis* spp. may make a non-negligible contribution to total biomass on the DDS regime. Temperatures were markedly colder on the shelf compared to the basin, with a cutoff at about 2°C in our in situ dataset, which is likely partly due to the presence of sea ice, and partly because the waters on both shelves are derived from the arctic, via the Labrador and Greenland currents in the west and east, respectively (Lazier, 1982). This temperature threshold was increased in the summer, when sea-surface temperatures increase over the entire LS, to a maximum value of 6°C . Our work is consistent with the biogeography of the LS inferred by Fragoso et al. (2016) who found a marked difference in terms of oceanographic conditions and phytoplankton assemblage composition between the shelves and the Labrador Basin. However, our more recently collected data revealed the presence of high biomass of *Phaeocystis* spp. in the LS in both 2015 and 2022 due, perhaps, to an as yet unidentified change in environmental conditions.

The use of satellite-derived Chl-a and SST allowed tracking of the boundaries of the oceanographic regimes all year long. The timing of the DFO monitoring cruises was dictated by logistical constraints, and while not ideal, this provided the opportunity to collect samples between early May and early July, covering a wide range of Chl-a (0.057 to 13.5 mg m^{-3}) and SST (-1.6 to 12.0°C) capturing the seasonal dynamics of the LS, from the productive shelves and the spring bloom to the low Chl-a summer conditions in the central LS. Time series analysis of ocean colour data in the LS have revealed a long spring bloom without a secondary fall bloom (Ringuette et al., 2022), unlike at intermediate latitudes in the Northwest Atlantic (Casault et al., 2024). This lack of a fall bloom is likely due to light limitation. Our in situ dataset did not cover the fall or winter seasons, resulting in uncertainties in primary production estimates during those periods, but given the low light levels at those times of year the contributions to annual primary production may be low.

The differences in taxonomic composition of the phytoplankton in the different oceanographic regimes is reflected in their differences in photosynthetic parameters. Cota et al. (1994) found that *Phaeocystis* spp. PI parameters may be an order of magnitude higher than other

phytoplankton mixed populations. In the current study, the average PI parameters in the HPB regime were similar to those in the MPB regime. In general, our α^B were similar to the ones found by Fragoso et al. (2017) with the lowest value found when *Phaeocystis* spp. was present and the largest values occurring in diatom dominated environment. On the other end, our P_{max}^B were much larger than the ones found by Fragoso et al. (2017), which is explain by the model fitting that was used in the studies. In the current study, we used a new model (<https://arxiv.org/abs/2412.17923>) to fit the PI curves, which results in higher P_{max}^B than current model. However, in agreement with Fragoso et al. (2017) the higher values were found in diatom/*Phaeocystis* spp. dominated waters while the lowest values were found in low chlorophyll-a environment. In general, diatom dominated populations located on the shelves had the highest photosynthetic efficiency, likely due to the ability of diatoms to thrive in turbulent, nutrient-rich environments with high variations in light intensity (Thomas et al., 1978; Lavaud, 2007; Inomura et al., 2023) as encountered on the Labrador and Greenland Shelves. Our results are also consistent with Harrison and Li (2015) who also found the highest photosynthetic parameters on the Shelves.

4.2. Daily PP in the LS between 2014 and 2022 and contribution of *Phaeocystis* spp. blooms to the annual PP budget

In general, the range of variation of PP estimates (both in situ and satellite) are consistent with estimates from Smith et al. (1991) who found daily PP in the order of 500 to $8000 \text{ mg C m}^{-2} \text{ d}^{-1}$ and Harrison and Li (2015) who found daily PP between 500 and $2000 \text{ mg C m}^{-2} \text{ d}^{-1}$ in the LS. Daily primary production in the LCB regime was also similar to measurements carried out on mixed population of phytoplankton in the Barents Sea (480 to $1200 \text{ mg C m}^{-2} \text{ d}^{-1}$) by Smith et al. (1991).

Comparison between in situ and satellite-derived primary production showed good agreement (slope 0.9, intercept of 0.22 and RMSLE of 0.22) despite some assumptions made in the satellite-based PP model. For instance, we used the mean of all the surface photosynthetic parameters for a given regime and an homogenous Chl-a profile derived from the satellite surface Chl-a, while the in situ PP was computed using α^B and P_{max}^B at both depths (with the deep parameters reassigned to the mixed layer depth, and interpolated between depths) and the true profile derived from the Chl-a fluorometer sensor mounted on the CTD. About 69 % of variance in the difference between the in situ and satellite PP can be explained by uncertainties in satellite-derived Chl-a (38 %) and P_{max}^B (17 %) and their combined effect, while the difference in α^B between the mean for a given regime and the in situ value did not show a significant relationship with the difference in PP. Note that out of the 39 sets of surface PI parameters, eight exhibited a photoinhibition response to high levels of irradiance. Photoinhibition was not, however, included in our model as it did not exhibit any relationship with phytoplankton community structure and could not be related to any oceanographic regime or satellite information (i.e., Chl-a, SST or PAR).

The Annual primary production budget in the LS varied between about 200 and 300 Tg of carbon between 2014 and 2022 with a mean annual production of 255 Tg of carbon. Sathyendranath et al. (1995) found a production value of 507 gC m^{-2} for the Polar Boreal biogeochemical province (Longhurst, 2007), which encompasses the Labrador Sea; scaling their results to the surface area of our region of interest gives a total annual production of about 800 Tg C y^{-1} , which is much larger than our estimate. While Sathyendranath et al. (1995) excluded coastal pixels given the poor performance in this type of water by the Coastal Zone Colour Scanner, these differences could be explained by the method used by Sathyendranath et al. (1995) to replace missing pixels with monthly means, such that missing pixels due to sea-ice may have been included in the annual budget and influenced the average production per meter squared. In addition, the seasonal α^B in their study was at the upper range of the values found here ($\sim 0.1 \text{ mgC [mg Chl-a]} \text{ h}^{-1} [\text{W m}^{-2}]^{-1}$ and between 0.07 and $0.1 \text{ mgC [mg Chl-a]} \text{ h}^{-1} [\text{W}$

$\text{m}^{-2}]^{-1}$ in this study). Our estimates are similar to the estimates from Harrison and Li (2015) who found annual primary production ranging from 209 to 249 Tg C y^{-1} (scaling their finding to the surface area used in this study) in the LS using satellite observations made by the Sea-viewing Wide Field-of-view Sensor (SeaWiFS) in the 2000s, and a different set of PI parameters for the Labrador and Greenland Shelves and Central Labrador Sea, based on in situ experiments carried out between 1991 and 2011.

Our study provides an insight in the seasonal cycle of phytoplankton primary production in the Labrador Sea and associated shelves. While the productivity per meter squared peaked in late spring or early summer for all oceanographic regimes (Fig. 5), the contribution of a given regime to annual production was driven by its spatial extent, such that the month at which a given regime peaked in absolute primary production did not necessarily correspond to its maximum contribution to annual production (Table 5). For instance, the maximum primary production of the DDS regime (in Tg) occurred between May and July but the DDS regime highest percentage contribution to monthly primary production occurred in fall, except in 2021 when it occurred in May. A large proportion of the annual production in the Labrador Sea (32 to 60 % of annual production with a mean of 43 %, Table 5) was contributed by “medium” bloom conditions (i.e., Chl-a of 0.6 to 2 mg m^{-3}) when the assemblage of phytoplankton is mixed, but dominated by diatoms, *Phaeocystis* spp. and green algae, as indicated by the high ratios of Fuco, Chl-c3 and Chl-b to Chl-a. The productivity of this MPB regime peaked in June and July, which was also when its contribution to total production peaked. The second most productive regime was the DDS regime, dominated by diatoms, with a mean contribution of 24.5 % to annual production that peaked in May and June. The reduced range of variation in annual percent production of this regime (21 to 29 %) is due to its limited spatial extent, as the shelf is characterized by a temperature threshold and a maximum depth of 2000 m. The Labrador Basin, when described as an low Chl-a regime (i.e., Chl-a < 0.6 mg m^{-3}) exhibited the pigment signature of a mixed population dominated by green flagellates as indicated by the high ratio of chlorophyll-b and 19'-Hex to Chl-a and the lowest Fuco:Chl-a ratio. The seasonal productivity within this oceanographic regime was fairly constant and was explained by the Chl-a threshold imposed on its extent. The contribution to annual production varied between 12.4 (2016) and 31.5 % (2014, the only year when the LCB regime contribution was larger than the DDS) and was negatively correlated with the contribution to annual production of the MPB regime ($R = -0.91$ model-2 type regression, p -value <0.01), meaning that annual production in one of these two regimes occurred at the expense of the other. Finally, contribution to annual primary production by the HPB regime ranged between 5.9 and 20 %, although during the peak of the bloom (typically in May), it contributed up to 60 % of the monthly primary production, as observed in 2015.

4.3. Unusually large blooms of *Phaeocystis* spp. in 2015 and 2022

Phaeocystis spp. may account for between a third and two-thirds of primary production in polar oceans (Cota Glenn et al., 1994). While blooms have been well documented in the vicinity (Greenland and Barents Seas) since the early 1970s (Smith et al., 1991; Cota Glenn et al., 1994; Orkney et al., 2020), observations of *Phaeocystis* spp. blooms in the Labrador Sea were previously limited to the Greenland Shelf and slope in spring (Fragoso et al., 2018) and four fjords along the Labrador coast in summer (Simo-Matchim et al., 2017). Both studies identified *P. pouchetii* in agreement with the pigment signature of the HPB regime found here, indicating relatively high ratios of Chl-c₃, 19'-Hex and Fucoxanthin to Chl-a (Nichols et al., 1991; Ditullio et al., 2003). As the Fuco:Chl-a ratio is low in *P. globosa* (Wu et al., 2022), This suggests that this species was not present, which is in agreement with the global distribution of *Phaeocystis* spp. (Schoemann et al., 2005). In addition, the species *P. pouchetii* was identified by genomic analysis (i.e., 18S rRNA sequencing) on samples collected during a cruise occurring in the

vicinity of our 2022 mission but a week later (R. Stevens-Green, pers. comm.). We note also that the pigment signature of *Phaeocystis* spp. may be confounded by the presence of other prymnesiophytes such as the coccolithophore *Emiliania huxleyi* (Swan et al., 2016). On the other hand, however, the bright optical signature of coccolithophores is unmistakable in satellite imagery and has not been recorded in the Labrador Sea during large blooms, while *Phaeocystis* spp. has been identified by light microscopy, supporting the idea of the dominance of *Phaeocystis* spp.

The blooms of *Phaeocystis* spp. in 2015 and 2022 were remarkable for their total primary production (49.3 and 33.2 Tg C respectively), whereas the average annual *Phaeocystis* production between 2014 and 2021, omitting 2015, was 21.4 Tg C). While these two blooms lasted slightly longer (6 weeks) than the average (5 weeks) (Table 5), their high productivity resulted from their large spatial extents (Fig. 7). The blooms appear to initiate along the northern Greenland coast in early spring as noted by Wu et al. (2008) and to propagate southward to reach the southeastern part of the LS later in the year. Blooms of prymnesiophytes sometimes occur following spring diatom blooms, although they have sometimes coincided with or preceded spring diatom blooms (Dale et al., 1999; Rey et al., 2000). This was likely the case in 2015, when the largest bloom recorded between 2014 and 2022 spread over the entire LS at its maximum extent. The causes of such blooms are not the subject of the current study, but several studies have highlighted the increasing significance of *Phaeocystis* spp. at the expense of diatoms in a warming ocean (Bopp et al., 2005), as *Phaeocystis* spp. directly competes with diatoms for resources (Schoemann et al., 2005). In fact, the inverse relationship between the HPB regime and the MPB regime suggests competition between diatoms and prymnesiophytes in the LS. It has been suggested that zooplankton, which prefer to graze on diatoms rather than *Phaeocystis* spp. colonies, might contribute to the development of these unusually large blooms (Estep et al., 1990; Granéli et al., 1993; Hansen et al., 1993; Nissen and Vogt, 2021). The fate of carbon produced during these blooms remains poorly understood. Reigstad and Wassmann (2007) found low carbon export from *Phaeocystis* spp. blooms, in agreement with Wolf et al. (2016) who found limited sinking of *Phaeocystis* colonies in sediment traps in the Southern Ocean. However, hydrodynamic forcing, such as subduction and deep vertical mixing can entrain particulate organic carbon resulting from *Phaeocystis* blooms to the deep ocean (Lalande et al., 2011).

4.4. Concluding remarks

We propose a regionally-tuned satellite-based primary production model that identifies a number of oceanographic regimes within the Labrador Sea region and assigns photosynthetic parameters based on a broad characterisation of their phytoplankton communities. Our results provide a more accurate estimation of biologically-produced carbon in the Labrador Sea, especially when compared to a method that uses mean parameters (Table S1). The use of regime-specific parameters provided annual carbon estimates that were about 20 to 30 % higher than the estimates found using mean parameters. In particular in the DDS regime, annual phytoplankton production was about 50 % higher using regime-based parameters. The model may be improved by using non-homogenous phytoplankton biomass vertical profiles, additional in situ data on environmental properties, phytoplankton pigment concentrations and photosynthetic parameters. The recent launch of the Phytoplankton Aerosol Cloud Ecosystem satellite by NASA with hyperspectral capacities will enhance our ability to characterise phytoplankton composition and thus to fine-tune our model. Improvement in water-column integrated primary production may also be achieved by coupling ocean colour satellite information with BGC-Argo float (e.g., Bendtsen et al., 2023), which provide information on chlorophyll-a concentration and particulate organic carbon profile, to inform on carbon export and some aspects of the biological carbon pump (Frenger et al., 2024). Our approach allowed the quantification of carbon

production by *Phaeocystis* spp., in particular during two large blooms that occurred in 2015 and 2022. While the production during these blooms seemed relatively small compared to annual production (i.e., 15 to 20 %), the timing and intensity of these blooms in spring will certainly have altered the fate of carbon both for export and transfer to higher trophic levels during that period.

CRediT authorship contribution statement

E. Devred: Writing – original draft, Visualization, Supervision, Resources, Project administration, Methodology, Investigation, Data curation, Conceptualization. **S. Clay:** Writing – review & editing, Methodology, Investigation, Data curation. **M. Ringuette:** Writing – review & editing, Funding acquisition, Data curation. **T. Perry:** Writing – review & editing, Data curation. **M. Amirian:** Writing – review & editing, Validation, Methodology, Investigation, Data curation. **A. Irwin:** Writing – review & editing, Supervision, Investigation. **Z. Finkel:** Writing – review & editing, Supervision, Investigation, Funding acquisition.

Declaration of competing interest

The authors declare the following financial interests/personal relationships which may be considered as potential competing interests:

Emmanuel Devred reports financial support was provided by Fisheries and Oceans Canada. Zoe V. Finkel reports financial support was provided by Canada Research Chair. If there are other authors, they declare that they have no known competing financial interests or personal relationships that could have appeared to influence the work reported in this paper.

Acknowledgements

The work presented here has been supported by the Atlantic Zone Off-shelf Monitoring Program, we specially thank Erica Head, William Li and Glenn Harrison for the collection of HPLC and Photosynthetic measurements at the start of the time series presented in the study (2014–2017). We also thank the captains and crew of the Canadian Coast Guard who manned the CCGS Hudson and Amundsen as well as the captain and crew from the R/V Atlantis. Z.V. Finkel was supported by the Canada Research Chairs program.

Appendix A. Supplementary data

Supplementary data to this article can be found online at <https://doi.org/10.1016/j.rse.2025.114713>.

Data availability

Data and code will be made available on a public repository (e.g., GitHub for code).

References

- Alvera-Azcarate, A., Barth, A., Rixen, M., Beckers, J., 2005. Reconstruction of incomplete oceanographic data sets using empirical orthogonal functions. Application to the Adriatic Sea. *Ocean Model* 2005 (9), 325–346.
- Antoine, D., Andre, J.M., Morel, A., 1996. Ocean primary production: 2. Estimation at global scale from satellite (coastal zone color scanner) chlorophyll. *Global Biogeochem. Cycles* 10, 57–69.
- Assmy, P., Smetacek, V., 2009. Algal blooms. In: Schaechter, Moselio (Ed.), Encyclopedia of Microbiology, Third edition. Academic Press, pp. 27–41. <https://doi.org/10.1016/B978-012373944-5.00001-8>.
- Baker, C.A., Martin, A.P., Yool, A., Popova, E., 2022. Biological carbon pump sequestration efficiency in the North Atlantic: a leaky or a long-term sink? *Glob. Biogeochem. Cycles* 36, e2021GB007286. <https://doi.org/10.1029/2021GB007286>.
- Balaguru, K., Doney, S.C., Bianucci, L., Rasch, P.J., Leung, L.R., Yoon, J.H., Lima, I.D., 2018. Linking deep convection and phytoplankton blooms in the northern Labrador Sea in a changing climate. *PLoS One* 13 (1), e0191509. <https://doi.org/10.1371/journal.pone.0191509>. PMID: 29370224; PMCID: PMC5784959.
- Barton, A.D., Irwin, A.J., Finkel, Z.V., Stock, C.A., 2016. Anthropogenic climate change drives shift and shuffle in North Atlantic phytoplankton communities. *Proc. Natl. Acad. Sci. USA* 113, 2964–2969. <https://doi.org/10.1073/pnas.1519080113>.
- Behrenfeld, M.J., Falkowski, P.G., 1997. Photosynthetic rates derived from satellite-based chlorophyll concentration. *Limnol. Oceanogr.* 42. <https://doi.org/10.4319/lo.1997.42.1.0001>.
- Bélanger, S., Babin, M., Tremblay, J.-É., 2013. Increasing cloudiness in Arctic damps the increase in phytoplankton primary production due to sea ice receding. *Biogeoscience* 10, 4087–4101. <https://doi.org/10.5194/bg-10-4087-2013>.
- Bendtsen, J., Vives, C.R., Richardson, K., 2023. Primary production in the North Atlantic estimated from in situ water column data observed by Argo floats and remote sensing. *Front. Mar. Sci.* 10. <https://doi.org/10.3389/fmars.2023.1062413>.
- Bopp, L., Autum, O., Cadule, P., Alvain, S., Gehlen, M., 2005. Response of diatoms distribution to global warming and potential implications: a global model study. *Geophys. Res. Lett.* 32, 1–4. <https://doi.org/10.1029/2005GL023653>.
- Bouman, H., Platt, T., Sathyendranath, S., Stuart, V., 2005. Dependence of light-saturated photosynthesis on temperature and community structure. *Deep-Sea Res. I Oceanogr. Res. Pap.* 52 (7), 1284–1299. <https://doi.org/10.1016/j.dsri.2005.01.008>.
- Brewin, R.J.W., Tilstone, G., Jackson, T., Cain, T., Miller, P.I., Lange, P.K., Misra, A., Airs, R.L., 2017. Modelling size-fractionated primary production in the Atlantic Ocean from remote sensing. *Prog. Oceanogr.* 58, 130–149. <https://doi.org/10.1016/j.pocean.2017.02.002>.
- Bricaud, A., Morel, A., Prieur, L., 1981. Absorption by dissolved organic matter of the sea (yellow substance) in the UV and visible domains. *Limnology and Oceanography* 26. <https://doi.org/10.4319/lo.1981.26.1.00043>.
- Campbell, J.W., O'Reilly, J.E., 1988. Role of satellites in estimating primary productivity on the Northwest Atlantic continental shelf. *Cont. Shelf Res.* 8 (2), 179–204. [https://doi.org/10.1016/0278-4343\(88\)90053-2](https://doi.org/10.1016/0278-4343(88)90053-2).
- Casault, B., Beazley, L., Johnson, C., Devred, E., Head, E., 2024. Chemical and biological oceanographic conditions on the Scotian shelf and in the eastern gulf of Maine during 2022. *Can. Tech. Rep. Fish. Aquat. Sci.* 3589 vi + 72 p.
- Charrad, M., Ghazzali, N., Boiteau, V., Niknafs, A., 2014. NbClust: an R package for determining the relevant number of clusters in a data set. *J. Stat. Softw.* 61 (6), 1–36. <https://www.jstatsoft.org/v61/i06>.
- Clay, S., Peña, A., DeTracey, B., Devred, E., 2019. Evaluation of satellite-based algorithms to retrieve chlorophyll-a concentration in the Canadian Atlantic and Pacific oceans. *Remote Sens.* 11 (22), 2609. <https://doi.org/10.3390/rs11222609>.
- Clément, L., Frajka-Williams, E., von Oppeln-Bronikowski, N., Gosczko, I., de Young, B., 2023. Cessation of Labrador Sea convection triggered by distinct fresh and warm (sub)mesoscale flows. *J. Phys. Oceanogr.* 53, 1959–1977. <https://doi.org/10.1175/JPO-D-22-0178.1>.
- Cota Glenn, F., Smith Walker, O., Mitchell, B.G., 1994. Photosynthesis of *Phaeocystis* in the Greenlea Sea. *Limnol. Oceanogr.* 39. <https://doi.org/10.4319/lo.1994.39.4.00948>.
- Dale, T., Rey, F., Heimdal, B.R., 1999. Seasonal development of phytoplankton at a high latitude oceanic site. *Sarsia* 84, 419–435.
- Devred, E., Sathyendranath, S., Platt, T., 2007. Delineation of ecological provinces using ocean 23 colour radiometry. *Mar. Ecol. Prog. Ser.* 346, 1–13.
- Devred, E., Wilson, K.L., Perry, T., Hardy, M., Brosnahan, M., Ringuette, M., 2024. Identification and validation of phytoplankton taxonomic assemblages derived from pigment signatures using samples collected in the Labrador Sea from 2014 to 2022. *Can. Tech. Rep. Fish. Aquat. Sci.* 3596 viii + 55 p.
- Ditullio, G.R., Jones, D.R., Geesey, M.E., 2003. Dimethylsulfide Dynamics in the Ross Sea During Austral Summer. In: Biogeochemistry of the Ross Sea (eds G.R. Ditullio and R. B. Dunbar). <https://doi.org/10.1029/078ARS18>.
- Eppley, R.W., 1972. Temperature and phytoplankton growth in the sea. *Fish. Bull.* 70, 1063–1085.
- Estep, K.W., Nejstgaard, J.C., Skjoldal, H.R., Rey, F., 1990. Predation by copepods upon natural populations of *Phaeocystis pouchetii* as a function of the physiological state of the prey. *Mar. Ecol. Prog. Ser.* 67 (3), 235–249. <https://www.jstor.org/stable/24816777>.
- Fetterer, F., Stewart, J.S., Meier, W.N., 2023. MASAM2: Daily 4 km Arctic Sea Ice Concentration, Version 2., Boulder, Colorado USA. NSIDC: National Snow and Ice Data Center. <https://doi.org/10.7265/bqd9-vm28> [Accessed on March 29th, 2024].
- Fox, J., Behrenfeld, M.J., Haëntjens, N., Chase, A., Kramer, S.J., Boss, E., Karp-Boss, L., Fisher, N.L., Penta, W.B., Westberry, T.K., Halsey, K.H., 2020. Phytoplankton growth and productivity in the Western North Atlantic: observations of regional variability from the NAAMES field campaigns. *Front. Mar. Sci.* 7, 24. <https://doi.org/10.3389/fmars.2020.00024>.
- Fragoso, G.M., Poulton, A.J., Yashayaev, I.M., Head, E.J.H., Stinchcombe, M.C., Purdie, D.A., 2016. Biogeographical patterns and environmental controls of phytoplankton communities from contrasting hydrographical zones of the labrador sea. *Prog. Oceanogr.* 141, 212–226. <https://doi.org/10.1016/j.pocean.2015.12.007>.
- Fragoso, G.M., Poulton, A.J., Yashayaev, I.M., Head, E.J.H., Purdie, D.A., 2017. Spring phytoplankton communities of the Labrador Sea (2005–2014): pigment signatures, photophysiology and elemental ratios. *Biogeoscience* 14, 1235–1259. <https://doi.org/10.5194/bg-14-1235-2017>.
- Fragoso, G.M., Poulton, A.J., Yashayaev, I.M., Head, E.J.H., Geir, J., Purdie, D.A., 2018. Diatom biogeography from the Labrador Sea revealed through a trait-based approach. *Front. Mar. Sci.* 5. <https://doi.org/10.3389/fmars.2018.00029>.
- Frenger, I., Landolfi, A., Kvale, K., Somes, C.J., Oschlies, A., Yao, W., Koeve, W., 2024. Misconceptions of the marine biological carbon pump in a changing climate: thinking outside the “export” box. *Glob. Chang. Biol.* 30, e17124. <https://doi.org/10.1111/gcb.17124>.

- Gieskes, W.W.C., Leterme, S.C., Peletier, H., Edwards, M., Reid, P.C., 2007. Phaeocystis colony distribution in the North Atlantic Ocean since 1948, and interpretation of long-term changes in the Phaeocystis hotspot in the North Sea. *Biogeochemistry* 83 (1–3), 49–60. <https://doi.org/10.1007/s10533-007-9082-6>.
- Granéli, E., Granéli, W., Rabbani, M.M., Daugbjerg, N., Fransz, G., Roudy, J.C., Alder, V. A., 1993. The influence of copepod and krill grazing on the species composition of phytoplankton communities from the scotia Weddell Sea. *Polar Biol.* 13, 201–213. <https://doi.org/10.1007/BF00238930>.
- Gregg, W.W., Carder, K.L., 1990. A simple spectral solar irradiance model for cloudless maritime atmospheres. *Limnol. Oceanogr.* 35. <https://doi.org/10.4319/lo.1990.35.8.1657>.
- Hansen, F.C., Reckermann, M., Klein Breteler, W.C.M., Riegman, R., 1993. Phaeocystis blooming enhanced by copepod predation on protozoa: evidence from incubation experiments. *Mar. Ecol. Prog. Ser.* 102, 51–57.
- Harrison, W.G., Li, W.K.W., 2015. Primary production in the Labrador Sea and adjacent waters: Atlantic zone off-shelf monitoring program 1991–2011. *Can. Tech. Rep. Hydrogr. Ocean. Sci.* 307 viii + 40 p.
- Hayward, A., Pinkerton, M.H., Gutierrez-Rodriguez, A., 2023. PhytoClass: a pigment-based chemotaxonomic method to determine the biomass of phytoplankton classes. *Limnol. Oceanogr. Methods* 21, 220–241. <https://doi.org/10.1002/lom3.10541>.
- Head, E.J.H., Horne, E.P.W., 1993. Pigment transformation and vertical flux in an area of convergence in the north atlantic. *Deep-Sea Res. II* 40, 329–346.
- Hilborn, A., Costa, M., 2018. Applications of DINEOF to satellite-derived chlorophyll-a from a productive coastal region. *Remote Sens.* 10, 1449. <https://doi.org/10.3390/rs10091449>.
- Hubert, L., Morel, A., 1998. Light scattering and chlorophyll concentration in case 1 waters: A reexamination. *Limnology and Oceanography* 5. <https://doi.org/10.4319/lo.1998.43.5.0847>.
- Imamura, K., Pierella Karlusich, J.J., Dutkiewicz, S., Deutsch, C., Harrison, P.J., Bowler, C., 2023. High growth rate of diatoms explained by reduced carbon requirement and low energy cost of silica deposition. *J. Microbiol. Spectrum* 11 (3). <https://doi.org/10.1128/spectrum.03311-22>.
- IOCCG, 2022. In: Vandermeulen, R.A., Chaves, J.E. (Eds.), *Ocean Optics and Biogeochemistry Protocols for Satellite Ocean Colour Sensor Validation Volume 7.0. Aquatic Primary Productivity Field Protocols for Satellite Validation and Model Synthesis*. International Ocean-Colour Coordinating Group (IOCCG), Dartmouth, NS, Canada. <https://doi.org/10.25607/OPB-1835>, 201pp. (IOCCG Protocols Series, Volume 7.0).
- Jassby, A.D., Platt, T., 1976. Mathematical formulation of the relationship between photosynthesis and light for phytoplankton. *Limnol. Oceanogr.* 4. <https://doi.org/10.4319/lo.1976.21.4.0540>.
- Jeffrey, S.W., Mantoura, R.F.C., Wright, S.W., 1997. Phytoplankton pigments in oceanography: guidelines to modern methods. 661p. Paris: Unesco Publishing, 1997. *J. Mar. Biol. Assoc. UK* 77 (3), 918. <https://doi.org/10.1017/S0025315400036389>.
- Kyewalyanga, M., Platt, T., Sathyendranath, S., 1997. Estimation of the photosynthetic action spectrum implication for primary production models. *Mar. Ecol. Prog. Ser.* 146, 207–223.
- Lalande, C., Bauerfeind, E., Nöthig, E.-M., 2011. Downward particulate organic carbon export at high temporal resolution in the eastern Fram Strait: influence of Atlantic water on flux composition. *Mar. Ecol. Prog. Ser.* 440, 127–136.
- Lancelot, C., Mathot, S., 1987. Dynamics of a Phaeocystis-dominated spring bloom in Belgian coastal waters. I. Phytoplanktonic activities and related parameters. *Mar. Ecol. Prog. Ser.* 37, 239–248.
- Lavaud, J., 2007. Fast regulation of photosynthesis in diatoms: mechanisms, evolution and ecophysiology. *Funct. Plant Sci. Biotechnol.* 1, 267–287.
- Lazier, J.R., 1982. Seasonal variability of temperature and salinity in the Labrador current. *J. Mar. Res.* 40 (S). https://elischolar.library.yale.edu/journal_of_marine_research/1647.
- Lee, Z.P., Carder, K.L., Marra, J., Steward, R.G., Perry, M.J., 1996. Estimating primary production at depth from remote sensing. *Appl. Opt.* 35 (3), 463–474.
- Legendre, L., Le Févre, J., 1995. Microbial food webs and the export of biogenic carbon in oceans. *Aquat. Microb. Ecol.* 9, 69–77.
- Liu, X., Wang, M., 2019. Filling the gaps of missing data in the merged VIIRS SNPP/NOAA-20 ocean color product using the DINEOF method. *Remote Sens.* 11, 178. <https://doi.org/10.3390/rs11020178>.
- Longhurst, A.R., 2007. Ecological Geography of the Sea, 2nd ed. Academic Press, London. <https://doi.org/10.1016/B978-0-12-455521-1.X5000-1>.
- Longhurst, A., Sathyendranath, S., Platt, T., Caverhill, C., 1995. An estimate of global primary production in the ocean from satellite radiometer data. *J. Plankton Res.* 17 (6), 1245–1271. <https://doi.org/10.1093/plankt/17.6.1245>.
- Morel, A., 1974. Optical properties of pure water and pure seawater, in: *Optical aspects of Oceanography*. Academic, New York, pp. 1–24.
- Mutshinda, C.M., Finkel, Z.V., Irwin, A.J., 2024. Large, regionally variable shifts in diatom and dinoflagellate biomass in the North Atlantic over six decades. *bioRxiv* 2024.07.02.601152. <https://doi.org/10.1101/2024.07.02.601152>.
- Nichols, P.D., Skerratt, J.H., Davidson, A., Burton, H., McMeekin, T.A., 1991. Lipids of cultured Phaeocystis pouchetii: signatures for food-web, biogeochemical and environmental studies in Antarctica and the Southern Ocean. *Phytochemistry* 30 (10), 3209–3214. [https://doi.org/10.1016/0031-9422\(91\)83177-M](https://doi.org/10.1016/0031-9422(91)83177-M).
- Nissen, C., Vogt, M., 2021. Factors controlling the competition between Phaeocystis and diatoms in the Southern Ocean and implications for carbon export fluxes. *Biogeoscience* 18 (251–283), 2021. <https://doi.org/10.5194/bg-18-251-2021>.
- Orkney, A., Platt, T., Narayanaswamy, B.E., Kostakis, I., Bouman, H.A., 2020. Bio-optical evidence for increasing Phaeocystis dominance in the Barents Sea. *Phil. Trans. R. Soc. A* 378, 20190357. <https://doi.org/10.1098/rsta.2019.0357>.
- Oziel, L., Baudena, A., Ardyna, M., Massicot, P., Randelhoff, A., Sallée, J.B., Ingvaldsen, R.B., Devred, E., Babin, M., 2020. Faster Atlantic currents drive poleward expansion of temperate phytoplankton in the Arctic Ocean. *Nat. Commun.* 11 (1), 1705. <https://doi.org/10.1038/s41467-020-15485-5>. PMID: 32249780; PMCID: PMC7136244.
- Peter, K.H., Sommer, U., 2013. Phytoplankton cell size reduction in response to warming mediated by nutrient limitation. *PLoS One* 8 (9), e71528. <https://doi.org/10.1371/journal.pone.0071528>.
- Platt, T., 1986. Primary production of the ocean water column as a function of surface light intensity: algorithms for remote sensing. *Deep-Sea Res.* 33 (2), 149–163.
- Platt, T., Sathyendranath, S., 1988. Oceanic primary production: estimation by remote sensing at local and regional scales. *Science* 241, 1613–1620.
- Platt, T., Sathyendranath, S., Forget, M.-H., White III, G.N., Caverhill, C., Bouman, H., Devred, E., Son, S., 2008. Operational estimation of primary production at large geographic scales. *Remote Sens. Environ.* 112, 3437–3448.
- Platt, T., Caverhill, C., Sathyendranath, S., 1991. Basin-scale estimates of oceanic primary production by remote sensing: The North Atlantic. *J. Geophys. Res.* 96 (C8), 15147–15159. <https://doi.org/10.1029/91JC01118>.
- Pope, M., Fry, E.S., 1997. Absorption spectrum (380–700 nm) of pure water. II. Integrating cavity measurements. *Appl. Opt.* 36, 8710–8723.
- R Core Team, 2023. R: A Language and Environment for Statistical Computing.. R Foundation for Statistical Computing, Vienna, Austria. <https://www.R-project.org/>.
- Reigstad, M., Wassmann, P., 2007. Does Phaeocystis spp. contribute significantly to vertical export of organic carbon? *Biogeochemistry* 83, 217–234.
- Rey, F., Noji, T.T., Miller, L.A., 2000. Seasonal phytoplankton development and new production in the Central Greenland Sea. *Sarsia* 85, 329–344.
- Ringuette, M., Devred, E., Azetsu-Scott, K., Head, E., Punshon, S., Casault, B., Clay, S., 2022. Optical, chemical, and biological oceanographic conditions in the Labrador Sea between 2014 and 2018. *DFO Can. Sci. Advis. Sec. Res. Doc.* 2022/021. v + 38 p.
- Robinson, A., Bouman, H.A., Tilstone, G.H., Sathyendranath, S., 2018. Size class dependent relationships between temperature and phytoplankton photosynthesis-irradiance parameters in the Atlantic Ocean. *Front. Mar. Sci.* 4. <https://doi.org/10.3389/fmars.2017.00435>.
- Roy, S., Llewellyn, C.A., Egeland, E.S., Johnsen, G. (Eds.), 2011. *Phytoplankton Pigments: Characterization, Chemotaxonomy and Applications in Oceanography*. Cambridge University Press.
- Rühs, S., Oliver, E.C.J., Biastoch, A., Böning, C.W., Dowd, M., Getzlaff, K., et al., 2021. Changing spatial patterns of deep convection in the subpolar North Atlantic. *J. Geophys. Res. Oceans* 126, e2021JC017245. <https://doi.org/10.1029/2021JC017245>.
- Ryan-Keogh, T.J., Thomalla, S.J., Chang, N., Moalusi, T., 2023. A new global oceanic multi-model net primary productivity data product. *Earth Syst. Sci. Data* 15, 4829–4848. <https://doi.org/10.5194/essd-15-4829-2023>.
- Sathyendranath, S., Longhurst, A., Caverhill, C.M., Platt, T., 1995. Regionally and seasonally differentiated primary production in the North Atlantic. *Deep Sea Res. I* 42 (10), 1773–1802. [https://doi.org/10.1016/0967-0637\(95\)00059-F](https://doi.org/10.1016/0967-0637(95)00059-F).
- Sathyendranath, S., Platt, T., 1997. Analytic model of ocean color. *Appl. Opt.* 36, 2620–2629.
- Sathyendranath, S., Cota, G., Stuart, V., Maass, H., Platt, T., 2001. Remote sensing of phytoplankton pigments: a comparison of empirical and theoretical approaches. *Int. J. Remote Sens.* 22 (2–3), 249–273. <https://doi.org/10.1080/014311601449925>.
- Schoemann, V., Bequevert, S., Stefels, J., Rousseau, V., Lancelot, C., 2005. Phaeocystis blooms in the global ocean and their controlling mechanisms: a review. *J. Sea Res.* 53, 43–66. <https://doi.org/10.1016/j.seares.2004.01.008>.
- Simo-Matchim, A.G., Gosselin, M., Poulin, M., Ardyna, M., Lessard, S., 2017. Summer and fall distribution of phytoplankton in relation to environmental variables in Labrador fjords, with special emphasis on Phaeocystis pouchetii. *Mar. Ecol. Prog. Ser.* 572, 19–42. <https://doi.org/10.3354/meps12125>.
- Stuart, V., Head, E.J.H., 2005. The BIO method. In *The Second SeaWiFS HPLC Analysis Round-Robin Experiment (SeaHARRE-2)*, ed. S. B. Hooker (NASA/TM 2005-212785, Greenbelt, Maryland). 112.
- Sirjacobs, D., Alvera-Azcárate, A., Barth, A., Lacroix, G., Park, Y., Nechad, B., Ruddick, K., Beckers, J., 2011. Cloud filling of ocean color and sea surface temperature remote sensing products over the southern North Sea by the data interpolating empirical orthogonal functions methodology. *J. Sea Res.* 65, 114–130.
- Smith, W.O., Trimborn, S.Y.R., 2024. Phaeocystis: a global enigma. *Annu. Rev. Mar. Sci.* 16, 417–441. <https://doi.org/10.1146/annurev-marine-022223-025031>.
- Smith, W.O., Codispoti, L., Nelson, D., et al., 1991. Importance of Phaeocystis blooms in the high-latitude ocean carbon cycle. *Nature* 352, 514–516. <https://doi.org/10.1038/352514a0>.
- Smith, W.O., Zhang, W.F., Hirzel, A., Stanley, R.M., Meyer, M.G., et al., 2021. A regional, early spring bloom of Phaeocystis pouchetii on the New England continental shelf. *J. Geophys. Res. Oceans* 126, e2020JC016856.
- Stuart, V., Sathyendranath, S., Head, E.J.H., Platt, T., Irwin, B., Maass, H., 2000. Bio-optical characteristics of diatom and prymnesiophyte populations in the Labrador Sea. *Mar. Ecol. Prog. Ser.* 201, 91–106.
- Swan, C.M., Vogt, M., Gruber, N., Laukoetter, C., 2016. A global seasonal surface ocean climatology of phytoplankton types based on CHEMTAX analysis of HPLC pigments. *Deep Sea Res. Pt. I* 109, 137–156. <https://doi.org/10.1016/j.dsr.2015.12.002>.
- Tesdal, J.E., Ducklow, H.W., Goes, J.I., Yashayaev, I., 2022. Recent nutrient enrichment and high biological productivity in the Labrador Sea is tied to enhanced winter convection. *Prog. Oceanogr.* 206, 102848. <https://doi.org/10.1016/j.pocean.2022.102848>.

- Thomas, W.H., Dodson, A.N., Reid, F.M.H., 1978. Diatom productivity compared to other algae in natural marine phytoplankton assemblages. *J. Phycol.* 14, 250–253. <https://doi.org/10.1111/j.1529-8817.1978.tb00294.x>.
- Ulloa, O., Sathyendranath, S., Platt, T., 1994. Effect of the particle-size distribution on the backscattering ratio in seawater. *Appl. Opt.* 33, 7070–7077.
- van Oostende, M., Hieronymi, M., Krasemann, H., Baschek, B., 2023. Global Ocean colour trends in biogeochemical provinces. *Front. Mar. Sci.* 10. <https://doi.org/10.3389/fmars.2023.1052166>.
- Volk, T., Hoffert, M.I., 1985. In: Ocean Carbon Pumps: Analysis of Relative Strengths and Efficiencies in Ocean-Driven Atmospheric CO₂ Changes, vol. 32. American Geophysical Union, Washington D.C., p. 9. <https://doi.org/10.1029/GM032p0099>
- Wang, Z., Brickman, D., Greenan, B.J.W., Yashayaev, I., 2016. An abrupt shift in the Labrador Current System in relation to winter NAO events. *J. Geophys. Res. Oceans* 121, 5338–5349. <https://doi.org/10.1002/2016JC011721>.
- Wang, S., Moore, J.K., 2011. Incorporating *Phaeocystis* into a Southern Ocean ecosystem model. *J. Geophys. Res. Oceans* 116, C01019.
- Wijesekera, H.W., Gregg, M.C., 1996. Surface layer response to weak winds, westerly bursts, and rain squalls in the western Pacific warm pool. *J. Geophys. Res.* 101 (C1), 977–997. <https://doi.org/10.1029/95JC02553>.
- Wolf, C., Iversen, M., Klaas, C., Metfies, K., 2016. Limited sinking of *Phaeocystis* during a 12 days sediment trap study. *Mol. Ecol.* 25, 3428–3435. <https://doi.org/10.1111/mec.13697>.
- Wu, Y., Platt, T., Tang, C.C.L., Sathyendranath, S., 2008. Regional differences in the timing of the spring bloom in the Labrador Sea. *Mar. Ecol. Prog. Ser.* 355, 9–20. <https://doi.org/10.3354/meps07233>.
- Wu, N., Fu, S., Song, X., et al., 2022. Stress regulation of photosynthetic system of *Phaeocystis globosa* and their hemolytic activity. *J. Oceanol. Limnol.* 40, 2164–2177. <https://doi.org/10.1007/s00343-022-1385-x>.
- Yashayaev, I., Loder, J.W., 2016. Recurrent replenishment of Labrador Sea Water and associated decadal-scale variability. *J. Geophys. Res. Oceans* 121, 8095–8114. <https://doi.org/10.1002/2016JC012046>.